EPHB2 promotes diet-induced MASH liver fibrosis

Masaaki Yoshigi[1,2#] Severin Donald Kamdem[3#], Ernest M. Kameni[1], Estelle Atiogue[1], Sarah Pellizzari[3], Francis Sprouse[4], Kimberley J. Evason[5], My N. Helms[6], Michael Goodman[7], Shuang Wang[8], Jisun So[9], Hyun Cheol Roh[9], Sihem Boudina[7], Mark Henkemeyer[4] and Patrice N. Mimche[1,2*]

[#]*Equal contribution*

*Correspondence

Affiliations

[1]*Department of Dermatology, Indiana University School of Medicine, Indianapolis IN 46202, USA*

[2]*Department of Medicine, Division of Gastroenterology and Hepatology, Indiana University School of Medicine, Indianapolis, IN46202, USA*

[3]*Department of Pathology, Division of Microbiology & Immunology, University of Utah, Salt Lake City, UT 84112, USA*

[4]*Department of Neuroscience, Kent Waldrep Foundation Center for Basic Research on Nerve Growth and Regeneration, Peter O'Donnell Jr. Brain Institute, UT Southwestern Medical Center, Dallas, TX 75390, USA*

[5]*Department of Pathology, Huntsman Cancer Institute, University of Utah, Salt Lake City, UT 84112, USA*

[6]*Department of Internal Medicine, Division of Respiratory, Critical Care and Occupational Pulmonary Medicine, University of Utah, Salt Lake City, UT84132, USA*

[7]*Department of Nutrition and Integrated Physiology, University of Utah, Salt Lake City, UT 84112, USA*

[8]*Division of Liver Diseases, The Icahn School of Medicine at Mount Sinai, New York, NY 10029, USA*

[9]*Department of Biochemistry and Molecular Biology, Indiana University School of Medicine, Indianapolis*

***Corresponding author:**

Patrice N Mimche
Department of Dermatology
Department of Medicine
Division of Gastroenterology and Hepatology, Indiana University School of Medicine
980 W Walnut St-R3 Building| Suite C634
TEL: +1-317-278-2059 |Email:pmimche@iu.edu

Abstract

The EphB2 receptor tyrosine kinase is thought to participate in numerous fibroinflammatory disorders. In metabolic dysfunction-associated steatohepatitis (MASH), we find EphB2 becomes upregulated in activated hepatic stellate cells (HSCs) from humans with the disease and from mice fed liver-injuring high fat diets. Genetic deletion or point mutation that inactivates the EphB2 tyrosine kinase domain in mice mitigated diet-induced liver inflammation and fibrosis, whereas a catalytically overactive point mutant mouse developed exacerbated steatosis and hepatic damage. Silencing *EPHB2* in primary human HSCs dampened the ability of TGFβ/SMAD signaling to activate the transdifferentiation of quiescent HSCs into profibrotic myofibroblasts, while HSC-specific deletion of the receptor, but not hepatocyte deletion, reduced liver scarring in multiple mouse models, even after fibrosis was established. Our studies demonstrate EphB2 forward signaling participates with TGFβ/SMAD signaling to bring about the pathogenesis of diet-induced fatty liver disease. Therapeutically targeting this receptor tyrosine kinase could counter MASH fibrosis.

Introduction

Metabolic dysfunction-associated steatohepatitis (MASH) is a chronic inflammatory/fibrotic disease that stems from progressive worsening of metabolic dysfunction-associated steatotic liver disease (MASLD). Viewed together, MASLD and MASH have become the most prevalent liver disease in developed nations due to the rise in type 2 diabetes and obesity (Muzurović et al., 2025; Younossi et al., 2025). In MASH, the progressive accumulation of liver fat (steatosis) and continual increasing liver inflammation leads to a chronic downward spiral of increasing tissue fibrosis and liver injury that can advance to scarring, cirrhosis, and organ failure. Liver fibrosis in MASH is attributed to excessive activation of quiescent hepatic stellate cells (HSCs) by TGFβ/SMAD signals, which causes them to transdifferentiate into proliferating, profibrotic myofibroblasts that produce the excessive collagen and other extracellular matrix (ECM) material characteristic of liver fibrosis (Targher et al., 2017; Z. Younossi et al., 2017). Hepatic fibrosis is associated with poor outcome in patients with MASH (Hagström et al., 2017; Z. M. Younossi et al., 2017). Despite ongoing progress made in understanding the molecular mechanisms driving the progression of MASH, FDA-approved treatments are limited to the recently approved thyroid hormone receptor-β agonist and glucagon-like peptide-1 receptor agonists, both of which indirectly target fibrosis (Harrison et al., 2024; Newsome & Loomba, 2025; Sanyal et al., 2025). The identification of signaling pathways that directly participate in MASH fibrosis is needed to better target this disease, especially finding those that activate HSCs, will reveal additional therapeutic targets to exploit for future treatments. Single nucleus RNA-sequencing has recently identified potential cell-cell communication hubs critical for fibrosis development in advanced MASH, including the receptor tyrosine kinase EphB2 (Wang et al., 2023; Xiao et al., 2023), which we previously showed participates in liver fibrosis and scaring caused by infectious and chemical agents (Mimche et al., 2015; Mimche et al., 2018).

EphB2 is one of fourteen related Eph molecules that comprise the largest family of transmembrane receptor tyrosine kinases (EphA1-A8, A10 and EphB1-B4, B6). The

Eph receptors interact with Ephrin ligands, which are also tethered to the plasma membrane through either a glycosylphosphatidylinositol-linked moiety (EphrinA1-A5) or a transmembrane segment followed by a short intracellular tail (EphrinB1-B3) (Kania & Klein, 2016). As both the Eph and Ephrin molecules are membrane localized, their interactions typically occur at sites of cell-cell contact and result in the activation of bidirectional signal transduction cascades into both the receptor-expressing cell (forward signaling) and ligand-expressing cell (reverse signaling) (Pasquale, 2008). Prior literature suggests Eph-Ephrin interactions participate in diverse biological processes relevant to fibrogenesis (Wu et al., 2019), including cell migration/proliferation, epithelial-to-mesenchymal-transition (EMT), angiogenesis, inflammation, wound healing, and tissue remodeling (Coulthard et al., 2012; Egal et al., 2024; Gao et al., 2014; Giannopoulos et al., 2025). However, it remains poorly understood how EphB2 may participate in MASH fibrosis.

Here, we show that EphB2 expression is elevated in fibrotic livers from humans with MASH and in mice fed high fat MASH fibrosis-inducing diets. We find EphB2 is required for the development of fibrosis and that this is partly driven by EphB2-mediated forward signaling as point mutation that inactivates the tyrosine kinase domain mitigated disease pathology while point mutation that constitutively over-activates it exacerbated liver scaring. While EphB2 expression in hepatocytes did not appear to participate in MASH fibrogenesis, silencing the receptor in stellate cells blocked their ability to become activated and transdifferentiate into ECM-producing myofibroblasts in response to TGFβ *in vitro*, and dampened liver fibrosis *in vivo*. Overall, this work uncovers EphB2 forward signaling as a key mediator of HSCs activation by working with TGFβ/SMAD signaling to bring about liver fibrosis and scaring with potential implications for the treatment of MASH.

Results

EphB2 is upregulated in human and mouse fibrotic MASH livers

To confirm if hepatic EphB2 expression is correlated with the progression of fibrosis, we evaluated *EPHB2* mRNA levels in a publicly available transcriptomic dataset of patients with MASLD/MASH at various stages of fibrosis (Hoang et al., 2019). We found increased hepatic *EPHB2* transcripts at early stages of disease that progressively intensified to reach very high levels at fibrosis stage 4 (F4) in MASH (**Figure S1A**). Next, we stained liver biopsies of patients at different stage of fibrosis (F0-F4) with a phosphoEphB2 antibody (a readout of EphB2 signaling), finding that receptor activation is strongly elevated in advanced MASH fibrosis F4 (**Figure S1B, and C**). To ascertain that our findings in human with MASH correlates with murine models of diet-induced MASH, we analyzed an RNA sequencing dataset of livers from mice fed either a standard chow diet or the obesogenic Gubra Amylin NASH (GAN) diet for 20 weeks (Xiong et al., 2019) and found hepatic *Ephb2* transcripts to be strongly upregulated in GAN diet fed mice compared to chow fed mice (**Figure S1D**). We then assessed hepatic *Ephb2*, *Vim*, *Cd11b* mRNA levels in mice fed the GAN diet for 7, 12,18 and 26 weeks and found a significant progressive increase in mRNA expression of these genes, all reaching very high levels at week 26 (**Figure S1E**). A phospho-EphB2

specific antibody (pEphB2) showed higher levels of activated receptor protein in liver sections of mice fed the GAN diet compared to chow fed mice (**Figure S1F**). Finally, we assessed hepatic EphB2 and αSMA protein levels in mice fed the non-obesogenic choline-deficient L-amino acid high fat diet (CDAA-HFD) for 12 weeks and found increased EphB2 and αSMA proteins compared to standard chow fed mice (**Figure S1G**). Taken together, this data shows hepatic EphB2 expression becomes strongly elevated in humans with MASH and in mice that have consumed a liver-injuring MASH diet.

EphB2 deficiency mitigates diet-induced MASH fibrosis

To dissect the potential involvement of EphB2 in the development of MASH, we fed male *Ephb2*+/+ wild-type and whole-body *Ephb2-/-* knockout mice the GAN diet for 26 weeks and assessed the level of hepatic steatosis, inflammation, and fibrosis (Radhakrishnan et al., 2021). While the *Ephb2-/-* knockouts are normal appearing, long-lived adult mice, we found that they gained significantly less weight as they aged compared to their *Ephb2*+/+ littermate controls when fed either the GAN diet or standard chow diet (**Figure S2A and B**), this despite an increased food intake in mutant mice compared to the wild-types (data not shown). Liver-to-body weight ratio was significantly reduced in GAN-fed *Ephb2-/-* compared to *Ephb2*+/+ mice (**Figure S2C**), and glucose tolerance was significantly enhanced in the knockouts compared to wild-type (**Figure S2D**). These data indicate that EphB2 deficiency mitigates the metabolic syndrome associated with diet-induced obesity in mice.

Histologic assessment of liver sections from GAN diet fed *Ephb2*+/+ mice showed extensive steatosis (H&E staining) and collagen deposition (Trichrome staining), whereas GAN diet fed *Ephb2-/-* mice had greatly reduced steatosis and collagen deposition (**Figure 1A**). Plasma levels of alanine aminotransferase (ALT), a marker of liver dysfunction, and total cholesterol were both significantly reduced in GAN diet fed *Ephb2-/-* mice compared *to Ephb2*+/+ mice, with no statistical difference detected for plasma aspartate aminotransferase (AST) or triglycerides (**Figure 1B and C)**. For an unbiased analysis of hepatic gene expression, we performed bulk RNA-sequencing of the livers from GAN-diet fed mutant and wild-type animals and found that the top 25 genes significantly downregulated in *Ephb2-/-* mice were those implicated in fibrosis (e,g. *Col1a1, Col1a2, Col3a1, Vim, Col6a3,* and *Myof*) and inflammation (e.g *Clec7a, Cerk, Axl, Tlr4, H2-Q1, Lgals3,* and *Vcam1*) (**Figure 1D**). In contrast, it was generally noted the GAN fed *Ephb2-/-* mutants retained high expression of genes involved in normal liver function. Further analysis of the data verified that the signalling pathways significantly downregulated in GAN diet fed *Ephb2-/-* compared to *Ephb2*+/+ mice were those involved in fibrosis (such as ECM organisation, collagen formation, integrin cell surface interactions) and inflammation (such as interferon gamma and interferon beta signalling, cytokine signalling in immune system and Nlrp3 inflammasome) (**Figure 1E**). We next performed hepatic gene expression analysis by quantitative PCR of selected fibrotic (*Col1a1, Timp1, Edn, Acta2, Pdgfrβ,* and *Vim*) and

inflammatory (*Cd11b, Il-6, Tnf-α, Ccr2, Tgf-β1*, and *Tgf-β2*) markers, revealing that all of these genes were significantly downregulated in GAN diet fed *Ephb2-/-* compared *Ephb2*+/+ mice (**Figure 1F and G**). Immunophenotyping showed a significant reduction in hepatic macrophage subsets (CD11b+F4/80+ and CD11b+Gr1+ cells) in GAN fed *Ephb2-/-* compared to *Ephb2*+/+ mice, with no notable change in T (CD3) or B (CD19) cell populations (**Figure S3A and B**). Together, these data support the hypothesis that EphB2 directly participates in the pathogenesis of diet-induced MASH fibrosis with potential roles in bringing about steatosis, inflammation, and fibrosis.

Given the systemic nature of the germline *Ephb2* deletion and the reduced body weight of the knockouts fed the GAN diet, it is possible that the above improvement of MASH pathology detected in the knockouts is related to the reduced level of obesity also observed in these mice. We therefore assessed if EphB2 is required for the development of diet-induced hepatic fibrosis in a non-obese mouse model of MASH. Here, *Ephb2*+/+ and *Ephb2-/-* mice were fed the non-obesogenic choline deficient L-amino acid high fat diet (CDAA-HFD) for 12 weeks (Radhakrishnan et al., 2020). Histologic assessment of liver sections from *Ephb2*+/+ and *Ephb2-/-* mice on CDAA-HFD revealed no notable difference in the level of steatosis, however, collagen deposition was significantly diminished in the mutant livers (**Figure 1H**). No significant difference in the plasma levels of ALT or triglyceride was observed in CDAA-HFD fed *Ephb2-/-* compared to *Ephb2*+/+ mice (**Figure 1I and J**), however plasma level AST was significantly reduced in the mutants compared to wild-type (**Figure 1I**), while plasma cholesterol was significantly elevated in the mutants (**Figure 1J**). Consistent with reduced collagen deposition, hepatic hydroxyproline (a marker of collagen turnover) was found to be significantly reduced in the livers of CDAA-HFD fed *Ephb2-/-* compared to *Ephb2*+/+ mice (**Figure 1K**). Quantitative PCR assessment of hepatic gene expression of selected fibrotic and inflammatory markers showed a significant reduction of *Col1a1, Col6a2, Tgf-β1*, *Smad3*, and *Cd11b* in the livers of CDAA-HFD fed *Ephb2-/-* mice compared to *Ephb2*+/+ mice (**Figure 1L**). Furthermore, immunophenotyping of selected hepatic myeloid cell subsets showed a significant reduction of inflammatory monocyte (Ly6C+) and Kupffer cells (F4/80+) in the livers of CDAA-HFD fed mutant compared to wild-type mice (**Figure S3C**). Altogether, the data show that hepatic inflammation and fibrosis induced in the non-obesogenic CDAA-HFD model are mitigated by deletion of EphB2 expression.

EphB2 forward signaling promotes MASH fibrosis

To test the requirement for EphB2-mediated forward signaling in diet-induced MASH fibrosis, mice with point mutations in key residues of the EphB2 catalytic domain *Ephb2*$^{F620D/F620D}$ (kinase-overactive), *Ephb2*$^{K661R/K661R}$ (kinase-dead), and wild type littermate controls were fed the obesogenic GAN diet for 26 weeks. We found an elevated steatosis and collagen deposition in liver sections of GAN diet fed *Ephb2*$^{F620D/F620D}$ compared to wild type mice, whereas the *Ephb2*$^{K661R/K661R}$ mice appeared like the knockouts and showed much less steatosis and collagen deposition

(**Figure 2A**). However, a significant change in the level of hepatic hydroxyproline was not observed in these mice (**Figure 2B**). Plasma levels of ALT and AST were elevated in GAN diet fed *Ephb2*$^{F620D/F620D}$ compared to wild type mice and further diminished (significantly for ALT only) in GAN diet fed *Ephb2*$^{K661R/K661R}$ mice (**Figure 2C**). The same observation was noted with plasma levels of cholesterol and triglycerides which were significantly elevated in GAN diet fed *Ephb2*$^{F620D/F620D}$ compared to wild type mice and further diminished in GAN diet fed *Ephb2*$^{K661R/K661R}$ mice (**Figure 2D**). Liver to body weight ratio was also significantly increased in GAN-diet fed *Ephb2*$^{F620D/F620D}$ compared to wild type mice and further diminished in GAN-diet fed *Ephb2*$^{K661R/K661R}$ mice (**Figure 2E**). When assessing the mRNA levels of selected fibrotic (*Col1a1*, *Col3a1*, and *Col6a2*) and inflammatory (*Tgf-β1*, *Il-1β*, *Il-6*, and *Cd11b*) markers, we found that most of them were elevated in GAN diet fed *Ephb2*$^{F620D/F620D}$ compared to wild type mice and further diminished in GAN-diet fed *Ephb2*$^{K661R/K661R}$ mice (**Figure 2F**). Taken together, this data shows that EphB2-mediated tyrosine kinase forward signaling drives GAN diet-induced MASH fibrosis.

Given the obesogenic nature of the GAN diet and the reduced body weight observed in GAN fed *Ephb2*$^{K661R/K661R}$ mice compared to wild type and *Ephb2*$^{F620D/F620D}$ mice (data not shown) that might impact hepatic steatosis, inflammation and fibrosis, we proceed to test the potential involvement of EphB2-mediated forward signaling in the carbon tetrachloride (CCl_4) model of hepatic fibrosis in mice. Here, *Ephb2*$^{F620D/F620D}$ mice, *Ephb2*$^{K661R/K661R}$ mice and wild-type littermate controls were injected with CCl_4 (10%, 2µl/g) three times a week for 4 weeks and liver injury/inflammation and fibrosis were evaluated. Histological assessment of liver sections showed increased liver damage and collagen accumulation in the liver of CCl_4-treated *Ephb2*$^{F620D/F620D}$ compared to CCl_4-treated wild-type mice and *Ephb2*$^{K661R/K661R}$ mice (**Figure 2G**). This was confirmed by finding a significant increase in hepatic hydroxyproline in CCl_4-treated *Ephb2*$^{F620D/F620D}$ compared to CCl_4-treated wild type mice and *Ephb2*$^{K661R/K661R}$ mice (**Figure 2H**). Plasma levels of ALT and AST were elevated in CCl_4-treated *Ephb2*$^{F620D/F620D}$ mice compared to CCl_4-treated wild type animals and significantly decreased in CCl_4-treated *Ephb2*$^{K661R/K661R}$ mice (**Figure 2I**). Immunophenotyping of a subset of myeloid cells known to promote inflammation revealed that hepatic CD11c+ cells (cDC1), CD11b+ macrophages, and F4/80 Kupffer cells were all significantly elevated in CCl_4-treated *Ephb2*$^{F620D/F620D}$ compared to CCl_4-treated wild-type mice, and further diminished CCl_4-treated *Ephb2*$^{K661R/K661R}$ mice, confirming the strong inflammatory response observed in EphB2 kinase overactive mice when subjected to liver injury (**Figure 2J**). We further examined the level of fibrosis in these mice by assessing gene expression of selected profibrotic markers (*Col1a1*, *Col3a1*, *Acta2*, *Timp1*, *Col1a2* and *Col6a2*) and found that most of them were elevated in CCl_4-treated *Ephb2*$^{F620D/F620D}$ compared to CCl_4-treated wild type mice and further diminished in CCl_4-treated *Ephb2*$^{K661R/K661R}$ mice, supporting the trichrome and Sirius red histology findings (**Figure 2K**). Altogether, our data indicates EphB2-mediated forward signaling potentially facilitates hepatic fibrogenesis following diet-induced or chemical-induced injury to the liver.

Expression of EphB2 in hepatocytes is not required for MASH fibrosis

To test if EphB2 expression in hepatocytes is needed for the development of MASH fibrosis, we generated *Ephb2*$^{loxP/loxP}$ mice and bred them with Albumin-*Cre* mice to selectively delete EphB2 expression in hepatocytes. Mice hemizygous for the Cre allele and homozygous for *Ephb2*$^{loxP/loxP}$ allele are referred to as *Hep*$^{\Delta Ephb2}$ and *Ephb2*$^{loxP/loxP}$ control mice are referred to as *Hep*^{WT}. Eight- to ten-week-old male *Hep*$^{\Delta Ephb2}$ and *Hep*^{WT} mice were fed CDAA-HFD for 8 weeks, then sacrificed and the blood and livers collected for assessment of the fibrotic response. EphB2 immunofluorescence staining was reduced in liver sections of *Hep*$^{\Delta Ephb2}$ compared to *Hep*^{WT} mice, confirming deletion of EphB2 in hepatocytes (**Figure S4A**). However, histologic assessment of liver sections from *Hep*$^{\Delta Ephb2}$ and *Hep*^{WT} mice fed the CDAA-HFD showed no difference in steatosis (H&E) or collagen deposition (Trichrome) in these mice (**Figure S4B**). Furthermore, other than a slightly elevated ALT, all other tested parameters of fibrosis or inflammation indicated the *Hep*$^{\Delta Ephb2}$ livers appeared not different from the *Hep*^{WT} controls (**Figure S4C-I**). These data indicate selective deletion of EphB2 expression in hepatocytes does not alter the progression of MASH fibrosis in CDAA-HFD fed mice.

TGFβ induced EPHB2 expression in human HSCs is SMAD-dependent

To identify the main hepatic cell type that upregulates EphB2 expression in MASH fibrosis, we analyzed a publicly available single-nuclei RNA sequencing dataset of mice with advanced disease (Wang et al., 2023). The data showed *Ephb2* transcripts were mostly elevated in HSCs, while those for one of its transmembrane ligands, EphrinB2 (*Efnb2*), were mainly found in endothelial cells which make extensive contact with stellate cells and are known to communicate important cell-cell signals involved in fibrosis (**Figure 3A**). Next, we used immunofluorescence to stain for activated EphB2 (pEphB2) and αSMA (a marker of activated HSCs/myofibroblasts) in human liver biopsies sections from healthy and advanced MASH fibrosis patients. We found that compared to healthy liver, pEphB2 was strongly upregulated in human advanced MASH and colocalized with high levels of αSMA (**Figure 3B**). Taken together, these findings point to HSCs and their activated profibrotic myofibroblasts as the main hepatic cell type that upregulates EphB2 protein and potentiates its signaling in MASH.

In MASH fibrosis, TGF-β cytokines are thought to be the main driver that activates quiescent HSCs and signals them to transdifferentiate into ECM-producing myofibroblasts (Frangogiannis, 2020; Sun et al., 2021). We therefore sought to determine if TGF-β signaling impacts EphB2 expression in cultured primary HSCs. We found that stimulation of HSCs in a time course up to 48 hours with recombinant human TGF-β1 significantly upregulated *EPHB2* (6-12h), *ACTA2* (24-48h), and *COL1A2* (48h) mRNA levels as well as EPHB2, αSMA and pSMAD2/3 protein levels (**Figure 3C and D**). Not limited to TGF-β1, recombinant human TGF-β2 and TGF-β3 also upregulated *EPHB2* and *ACTA2* mRNA and protein in primary human HSCs (**Figure S5A and B**). We next investigated if the increased expression of EphB2 in HSCs stimulated by TGF-β was SMAD-dependent (Hata & Chen, 2016). Pharmacological blockade of TGF-β/SMAD signaling with selective inhibitions of TGF-β receptor type I (SD208 and SB525334) and SMAD3 (SIS3) strongly dampened TGF-β1-mediated upregulation of

EPHB2 mRNA in primary human HSCs (**Figure 3E**). Moreover, genetic inhibition of *SMAD2* and *SMAD3* using siRNA also blocked TGF-β1-mediated upregulation of *EPHB2* mRNA in HSCs (**Figure 3F**). We next analyzed a publicly available SMAD3 ChIP-sequencing dataset of TGF-β1 stimulated HSCs cell line (Ding et al., 2013) and found that SMAD binding elements (SBE) are present in the promoter of human *EPHB2* (**Figure 3G**). To validate the presence of SBE in the peak/promoter region of *EPHB2*, we performed a targeted SMAD3 ChIP-qPCR in control and TGF-β1 stimulated primary human HSCs and found that indeed SMAD3 occupied the *EPHB2* promoter region analyzed (**Figure 3H**).

EPHB2 is required for HSCs activation

The ability of TGF-β to activate quiescent HSCs to transdifferentiate into ECM-producing myofibroblasts is a hallmark of hepatic fibrosis (Friedman, 2008; Kisseleva, 2017; Wells & Schwabe, 2015). Given the above data that shows genetic deletion of EphB2 or point mutation inactivation of its tyrosine kinase catalytic domain mitigates HFD-induced MASH fibrosis and that EPHB2 is predominantly expressed in TGF-β1 activated HSCs, we reasoned that this receptor could be critical for hepatic stellate cell-to-myofibroblast phenoconversion (Mimche et al., 2018). To test this idea, we silenced *EPHB2* in primary human HSCs with siRNA and then stimulated with TGF-β1 for 48h. The data showed that compared to the control nontargeting siRNA HSCs, silencing *EPHB2* in HSCs strongly reduced its receptor gene expression (**Figure 4A**) and suppressed the ability of TGF-β to stimulate their transdifferentiation into myofibroblasts as documented by reduced expression of *ACTA2* and *COL1A1* mRNA levels (**Figure 4B**), and protein levels of EPHB2 and αSMA (**Figure 4C-D**). We also noticed that silencing *EPHB2* in HSCs increased SMURF2 protein (**Figure 4D**) as well as the mRNA levels of inhibitory SMADs (*SMAD7*, *SMURF1* and *SMURF2*) (**Figure S6A**) known to dampen TGFβ/Smad signaling (Miyazawa & Miyazono, 2017). Because EPHB2 is a transmembrane receptor tyrosine kinase, we reasoned the profibrotic activity of this protein could involve a potential interaction with TGFβ receptors. To address this possibility, we immunoprecipitated EphB2 from primary human HSCs and found that TGFβRII co-precipitated (**Figure 4E**). Proximity ligation assay confirmed that EPHB2 is indeed in the vicinity of TGFβRII (**Figure 4F**), lending support for a potential crosstalk between EPHB2 and TGFβRII in the regulation of TGFβ/Smad signaling in fibrogenesis. To further confirm a role of EPHB2 in TGFβ/SMAD signaling, silencing *EPHB2* in TGFβ1-stimulated HSCs for 1 hour attenuated pSMAD2/3 and pAKT (**Figure 4G**), which are required for myofibroblast activation (Son et al., 2009). Furthermore, we transduced primary human HSCs with a lentivirus expressing luciferase under the control of SBE and noticed that the luciferase activity was significantly reduced when *EPHB2* was silenced in TGF-β-stimulated HSCs for 3h compared to controls (**Figure 4H**). The data above solidifies an interconnection between EPHB2 and TGFβRII, with the two receptors working together to potentiate each other's expression/activity and to bring about the activation of HSCs.

Bulk RNA sequencing was then performed to gain insight in the signaling pathways that are affected when EPHB2 is silenced in TGF-β1 stimulated HSCs

compared to control cells. This revealed the top downregulated genes in *EPHB2* silenced TGFβ-stimulated HSCs were involved in fibrosis including *EPHB2, LTBP4, DES, COL14A1, COL15A1, TNC, POSTN, PIEZO2, COL12A1, TIMP3* (**Figure 4I**) which were validated by qPCR (**Figure S6B**). Several signaling pathways known to be involved in fibrogenesis, cell cycle/division, and migration/proliferation were downregulated in TGF-β1-stimulated HSCs that had EPHB2 silenced, including myogenesis, G2-M checkpoint, E2f targets, epithelial mesenchymal transition, mitotic spindle, and Myc Targets V1/V2 (**Figure 4J**). To identify the kinases that are altered when *EPHB2* is silenced in TGFβ-stimulated HSCs, we performed a global kinome mapping and found that CDKs, CDKLs, and MAPKs serine/threonine kinases (STK) were the main kinases dysregulated in *EPHB2* silenced TGF-β-stimulated HSCs compared to TGF-β-stimulated controls HSCs (**Figure S7**). Finally, as stellate cells actively migrate to injured areas of the liver to further spread ECM deposition and fibrosis, we subjected *EPHB2* silenced HSCs to wound healing assays and found significantly dampened migration compared to the control cells (**Figure 4K and L**). Altogether, the above data point to a critical interplay of EPHB2 and TGFβ/SMAD signaling that can affect biological processes important in MASH, such as cell differentiation and migration, that when combined, work to bring about the progression of hepatic fibrogenesis.

EphB2 deficiency in HSCs dampens MASH fibrosis

To better understand how EphB2 drives MASH fibrosis, $Ephb2^{loxP/loxP}$ mice were bred with tamoxifen-inducible $PdgfrβCre^{ERT2}$ mice to selectively delete its expression in HSCs (Henderson et al., 2013). Mice hemizygous for the Cre allele and homozygous for $Ephb2^{loxP/loxP}$ allele are referred to as $HSC^{ΔEphb2}$ and $Ephb2^{loxP/loxP}$ control mice are referred to as HSC^{WT}. $HSC^{ΔEphb2}$ and HSC^{WT} mice were administered tamoxifen by intraperitoneal (IP) injection for 5 consecutive days and then fed the CDAA-HFD for 8 weeks. Histologic assessment of liver sections from $HSC^{ΔEphb2}$ and HSC^{WT} mice fed the CDAA-HFD showed no change in the level steatosis (H&E), however, collagen deposition (Trichrome) was diminished in the liver sections of CDAA-HFD fed $HSC^{ΔEphb2}$ compared to HSC^{WT} mice (**Figure 5A**). The reduction of collagen deposition in $HSC^{ΔEphb2}$ mice was confirmed by a decreased hepatic hydroxyproline in the livers of CDAA-HFD fed $HSC^{ΔEphb2}$ compared to HSC^{WT} mice (**Figure 5B**). No significant difference in the plasma levels of ALT, AST, cholesterol, or triglycerides was observed in CDAA-HFD fed $HSC^{ΔEphb2}$ compared to HSC^{WT} mice (**Figure 5C and D**). Quantitative PCR assessment of hepatic gene expression of selected fibrotic markers showed a significant reduction of *Col1a1, and Col3a1* mRNA levels, while no difference in the mRNA level of inflammatory markers *Cd11b*, *Il-1β* and *Il-6* was observed in the livers of CDAA-HFD fed $HSC^{ΔEphb2}$ compared to HSC^{WT} mice (**Figure 5E and F**). To take an unbiased approach to uncover biological pathways that are affected by deletion of EphB2 in HSCs, bulk RNA sequencing was performed. We found that some of the top upregulated genes in CDAA-HFD fed HSC^{WT} compared to CDAA-HFD fed $HSC^{ΔEphb2}$ mice included *Lrg1*, *Egfr*, *Fgf1*, *Orm*1, *Lbp*, *Serpina3n*, *Saa2*, *Saa1*, and *Nt5e* which are

known to be upregulated in human MASH (**Figure 5G**) (Wang et al., 2023). Using pathways analysis, we noticed that biological processes implicated in fibrogenesis such as the epithelial mesenchymal transition, myogenesis, Notch signaling and Wnt/beta catenin signaling were downregulated in CDAA-HFD fed *HSC*$^{\Delta Ephb2}$ compared to HSC^{WT} mice (**Figure 5H**). However, inflammatory signalling pathways were mostly upregulated in CDAA-HFD fed *HSC*$^{\Delta Ephb2}$ compared to *HSC*^{WT} mice (**Figure 5H**). We then assessed the hepatic myeloid cell composition of CDAA-HFD fed *HSC*$^{\Delta Ephb2}$ and *HSC*^{WT} mice and found no significant difference in the levels of cDC1, Ly6C, PMN and F4/80 populations (**Figure 5I**).

Given that *Col1a2* was one of the top upregulated genes in mice fed the GAN diet (**Figure 1D**), we investigated the impact of deleting EphB2 in Col1a2 expressing HSCs on GAN diet-induced MASH fibrosis. We bred *Ephb2*$^{loxP/loxP}$ mice with the tamoxifen-inducible *Col1a2Cre*^{ERT2} mice to delete EphB2 expression in HSCs. Mice hemizygous for the Cre allele and homozygous for *Ephb2*$^{loxP/loxP}$ allele are referred to as *Cre*+ and the control *Ephb2*$^{loxP/loxP}$ mice without the Cre driver are referred to as *Cre-.* Both *Cre*+ and *Cre*- mice were administered tamoxifen IP for 5 consecutive days and then fed the GAN diet for 22 weeks. Histologic assessment of liver sections from GAN diet fed *Cre*+ and *Cre*- mice showed no change in the level steatosis (H&E staining), however, collagen deposition (Trichrome staining) was diminished in the livers of GAN diet fed *Cre*+ compared to *Cre*- mice (**Figure 6A**). Hepatic hydroxyproline content was significantly reduced in the liver of GAN fed *Cre*+ mice compared to *Cre*- mice (**Figure 6B**). However, we did not observe a significant difference in the plasma levels of ALT, AST or triglycerides in GAN fed *Cre*+ compared to *Cre*- mice (**Figure 6C and D**). In contrast, plasma level cholesterol was significantly reduced in GAN fed *Cre*+ compared to *Cre*- mice (**Figure 6D**). Also, there was no significant difference in the liver to body weight ratio between GAN diet fed *Cre*+ and *Cre*- mice (**Figure 6E**). Selected fibrotic maker mRNA levels such as *Acta2, Col1a1, Col1a2* were significantly reduced in GAN fed *Cre*+ compared to *Cre*- mice (**Figure 6F**), while there was no difference in mRNA levels of inflammatory markers *Cd11b*, *Il-1β*, *Il-6*, and *Cxcl-10* between GAN fed *Cre*+ and *Cre*- mice (**Figure 6G**). When evaluating immune cell infiltration in the livers of these mice, we noticed that there was no major difference in most hepatic myeloid cell subsets except for cDC1 and Ly6C+ cell populations that were significantly reduced in GAN fed *Cre*+ compared to *Cre*- mice (**Figure 6H**). Taken together, these data emphasize the role of EphB2 in HSC/myofibroblast activation *in vivo* as knocking down EphB2 using either *PdgfrβCre*^{ERT2} or C*ol1a2Cre*^{ERT2} drivers did not mitigate steatosis or inflammation, though both approaches clearly suppressed HFD-induced MASH fibrosis.

EphB2 deficiency in HSCs attenuates CCl_4-induced hepatic fibrosis.

To determine if EphB2 expression in HSCs also contributes to chemical induction of hepatic fibrosis, *Col1a2Cre*^{ERT2}*/Ephb2*$^{loxP/loxP}$ (*Cre+)* and *Ephb2*$^{loxP/loxP}$ (*Cre-*) mice were administered tamoxifen IP for 5 consecutive days and treated with CCl_4 three times a

week for 4 weeks. Histologic assessment of liver sections from CCl_4-treated *Cre*+ and *Cre*- mice showed a reduction in collagen accumulation in CCl_4-treated *Cre*+ compared to *Cre*- mice (**Figure S8A**). This was translated by a significant reduction in hepatic hydroxyproline content in the livers of CCl_4-treated *Cre*+ compared to *Cre*- mice (**Figure S8B**). However, no significant difference in the plasma levels of ALT and AST was observed in CCl_4-treated *Cre*+ and *Cre*- mice (**Figure S8C**). When assessing gene expression of selected fibrotic markers, we found that hepatic mRNA levels of *Col1a1*, *Fn1*, *Acta2*, and *Timp1* were significantly attenuated in CCl_4-treated *Cre*+ compared to *Cre*- mice (**Figure S8D**). In contrast, we found no significant difference in the hepatic mRNA levels of selected inflammatory markers evaluated (*Cd11b*, *Ccl5*, *Cxcl-10*, and *Il-1β*) in CCl_4-treated *Cre*+ compared to *Cre*- mice (**Figure S8E**). Finally, Immunophenotyping of selected hepatic immune cells know to contribute to inflammation (Koyama & Brenner, 2017) showed no significant difference in the levels of myeloid cells subsets mainly inflammatory monocytes (Ly6C+), neutrophils (PMN), kupffer cells (F4/80) as well as T (CD3) and B (CD19) cells in the livers of CCl_4-treated *Cre*+ compared to *Cre*- mice (**Figure S8F**). Taken together, these data solidify the concept that EphB2 expression in HSCs exclusively participate in HSCs-to-myofibroblasts transition, a major prerequisite for the development and progression of hepatic fibrosis.

Deletion of EphB2 in HSCs promotes regression of establish fibrosis

We finally investigated whether deletion of EphB2 could promote the regression of established fibrosis. Here, male *Col1a2Cre*^{ERT2}*/Ephb2*$^{WT/WT}$ (*Col*^{WT}*)* and *Col1a2Cre*^{ERT2}*/Ephb2*$^{loxP/loxP}$ (*Col*$^{\Delta Ephb2}$) mice (6 to 8 weeks of age) were fed the non-obesogenic CDAA-HFD for a total of 12 weeks to induce steatosis, lobular inflammation, and fibrosis. At week 8, after MASH fibrosis was established, animals were IP injected with tamoxifen each day for 1 week to delete EphB2 expression from activated HSCs, and then mice allowed to continue the CDAA-HFD diet for another 4 weeks (**Figure 7A**). Histologic assessment of resulting liver sections showed a strong reduction of collagen accumulation in the animals deleted for EphB2 (**Figure 7B**), that was associated with a significant reduction in hepatic hydroxyproline content (**Figure 7C**). However, no obvious difference in ALT, AST, cholesterol, or triglycerides was observed between the CDAA-HFD fed *Col*^{WT} control and *Col*$^{\Delta Ephb2}$ mice (**Figure 7D and E)**, even though the total hepatic mRNA level of *Ephb2* was significantly reduced in the EphB2-deleted animals (**Figure 7F**). Consistent with reduced collagen and hydroxyproline, gene expression of fibrotic markers *Acta2*, *Col1a1*, *Col1a2*, *Col3a1, Col6a2*, and *Pdgfrβ* were significantly attenuated in the CDAA-HFD fed *Col*$^{\Delta Ephb2}$ EphB2-deleted mice compared to the *Col*^{WT} controls (**Figure 7G**). In contrast, no significant difference was detected for selected inflammatory markers in the livers (*Cd11b*, *Il-6*, and *Tnf-α*) (**Figure 7H**). Taken together, these data show that deletion of EphB2 can promote the regression of fibrosis when MASH is already established.

Discussion

Fibrosis is associated with poor outcome in patients with MASH, and for this reason the identification of critical signaling pathways involved in fibrogenesis is a priority for the development of potential anti-scaring therapeutics. We have previously showed that the receptor tyrosine kinase EphB2 promotes the development of hepatic, renal and dermal fibrosis (Egal et al., 2024; Huang et al., 2021; Mimche et al., 2015; Mimche et al., 2018). Here, we report that EphB2 is upregulated in the livers from humans with advanced MASH and in murine models of MASH fibrosis. We have dissected the contribution of EphB2 in MASH fibrosis using clinically relevant murine models of MASH consisting of feeding mice either the obesogenic GAN diet for up to 26 weeks or the shorter acting non-obesogenic CDAA-HFD diet for 8-12 weeks. We found that global deletion of *Ephb2* in mice attenuated GAN diet-induced steatosis, inflammation and fibrosis likely because of the unexpected protection from obesity observed in these mice. However, in the non-obesogenic CDAA-HFD model of MASH, *Ephb2-/-* mice were only protected from inflammation and fibrosis. Our data positions EphB2 as a critical hub regulating steatosis, inflammation and fibrosis which are prerequisite for the development and progression of obesity-associated MASH fibrosis. How EphB2 regulates the obesogenic component of MASH fibrosis is currently under investigation.

Recent single-nucleus RNA sequencing data has uncovered critical cell-cell communication hubs in advanced MASH (Wang et al., 2023). Eph-Ephrin signaling becomes engaged at sites of cell-cell contact and when activated, leads to transduction of intracellular signals into both the receptor-expressing cell (forward signaling) and the ligand-expressing cell (reverse signaling). In a study profiling hepatic gene expression in patients with MAFLD/MASH, EphB-mediated forward signaling was uncovered as a top predictor of advanced MASH fibrosis (Hoang et al., 2019). However, a functional assessment of EphB2 forward signaling was not performed. Using EphB2 germline knockout and point mutant mice, we have functionally validated this observation by showing that steatosis, inflammation, and fibrosis were greatly elevated in GAN diet fed EphB2 kinase-overactive mice compared to the wild-type controls, while the GAN fed EphB2 kinase-dead mice mimicked some of the features of EphB2 knockouts mice and were protected from developing MASH fibrosis. Inflammation and fibrosis were also enhanced in CCl_4 chemically-injured EphB2 kinase-overactive mice compared to the wild type controls and, likewise, were attenuated in the EphB2 kinase-dead mice like the knockouts (Mimche et al., 2015; Mimche et al., 2018). These data support the requirement for EphB2 catalytic tyrosine kinase forward signaling in the development of MASH fibrosis. Future work will determine if EphrinB reverse signaling also participates in MASH.

Having established the critical role played by EphB2, and more specifically EphB2 forward signaling, in the development/progression of MASH fibrosis, we next investigated the molecular underpinnings of EphB2 signaling in MASH. In contrast to prior studies (Xiao et al., 2023), we found that hepatocytes expressing EphB2 were dispensable for diet-induced MASH fibrosis. This discrepancy could be likely due to the diets used to induce liver injury. In fact, we noticed that EphB2 was mostly elevated in HSCs in advanced MASH and its expression was upregulated by the TGFβ/SMAD signaling as illustrated by studies using genetic or pharmacological abrogation of this

profibrotic signaling system (Frangogiannis, 2020). The functional validation of the binding of SMAD complex in the putative promoter of human *EPHB2* further supports the involvement of the canonical TGFβ/SMAD signaling in the regulation of EphB2 expression in human HSCs. Moreover, we noted that siRNA silencing of *EPHB2* in HSCs blocked TGFβ-mediated HSCs-to-myofibroblasts transdifferentiation *in vitro*. This is likely due to the potential crosstalk between Eph/Ephrin and TGFβ/SMAD signaling as co-immunoprecipitation and proximity ligation assay experiments confirmed a plausible physical association and showed that EphB2 receptor molecules are in the vicinity of TGFβRII molecules. Knocking down *EPHB2* attenuated TGFβ-induced SMAD activation in human HSCs/myofibroblasts. Furthermore, RNA sequencing revealed that the top downregulated genes in TGF-β stimulated *EPHB2* deleted HSCs were mostly involved in fibrogenesis including *EPHB2* itself. Pathway analysis of RNA sequencing and global kinome mapping showed that biological processes involved in cell division, migration/proliferation and epithelial-to-mesenchymal transition were dampened in HSCs in the absence of EPHB2. Our data solidifies the contribution of EPHB2 in the activation/migration and proliferation of human HSCs during fibrogenesis. Overall, our mechanistic studies suggest a model whereby, EphB2 interacts with TGFβR2 to facilitate canonical TGFβ/SMAD signaling to drive HSCs/myofibroblasts activation, migration, and proliferation.

We have also functionally validated the requirement for EphB2 expression in HSCs for MASH fibrosis to occur *in vivo.* We have showed that targeted deletion of EphB2 in HSCs attenuated CDAA-HFD and GAN-diet induced fibrosis with no major changes in steatosis and inflammation relative to control mice. The same observation was also made in the CCl_4 model of hepatic fibrosis whereby targeted deletion of EphB2 in HSCs mitigated CCl_4-induced liver fibrosis without affecting inflammation. Furthermore, when MASH fibrosis was already established in mice, deletion of EphB2 promotes the regression of this pathology in mice, supporting ongoing effort to develop inhibitors of this receptor tyrosine kinase for the treatment of advanced MASH fibrosis. Taken together, we provide extensive data showing that EphB2 receptor is a *bona fide* driver of fibrogenesis in human HSCs *in vitro* and further translated *in vivo* by the significant reduction of fibrosis observed when EphB2 is deleted globally or specifically in HSCs in various murine models of MASH fibrosis. Our data provides a strong rationale for the development of EphB2-targeted therapeutics for the treatment of MASH.

Materials and Methods

Human samples

De-identified human livers samples from patients with MASLD/MASH at various stage of fibrosis (F0 – F4, modified Kleiner-Brunt staging methodology) (Kleiner & Brunt, 2012), reviewed by a liver pathologist, were obtained from the University of Utah Pathology Archives. The protocol was approved by the University of Utah Institutional

Review Board and determined to be exempt from human subjects' research (IRB # 00117459).

Mice:

Animal experiments were performed in compliance with guidelines of Indiana University Institution Animal Care and Use Committee (IACUC) protocol number 24131 MD/R/HZ/E/EX and University of Utah IACUC protocol number 1688. Male and female C57BL/6J mice [RRID:IMSR_JAX:000664], aged 8-12 weeks, were bred in-house or purchased from Jackson laboratory (Bar Harbor, ME). *Ephb2-/-* and littermate controls *(Ephb2+/+)* mice on the C57BL6/J background has been described previously (Henkemeyer et al., 1996) and bred in-house. *Ephb2*-kinase overactive mice (*Ephb2*$^{F620D/F620D}$) and *Ephb2*-kinase dead (*Ephb2*$^{K661R/K661R}$) originally in the CD1/129 background (Genander et al., 2009; Holmberg et al., 2006), were backcrossed for 10 generations into C57BL6/J strain. To generate hepatic stellate cells/mesenchymal stromal cells *Ephb2* knockout mice, *Ephb2*$^{loxP/loxP}$ mice were crossed with the tamoxifen-inducible Cre recombinase driven by mouse promoter *Col1a2Cre*^{ERT2} (RRID:IMSR_JAX :029235) or *PdgfrβCre*^{ERT2} (RRID:IMSR_JAX :029684). Hepatocyte-specific *Ephb2* knockout mice were generated by crossing *Ephb2*$^{loxP/loxP}$ mice with Alb-Cre mice (RRID:IMSR_JAX :003574). All the *Cre* mouse lines used in this study were purchased from Jackson Laboratories (Bar Harbor, ME). Littermates with floxed alleles but without Cre were used as wild type controls. Where appropriate, both Cre inducible mouse line and controls animals were administered tamoxifen 75mg/kg for 5-7 consecutive days and hepatic fibrosis induced a week later. All animals were housed in a specific pathogen-free environment, with no more than five animals per cage under controlled light (12h light and 12h dark cycle), temperature (24 ± 2ºC), humidity (50 ± 10%) conditions, and provided water and food *ad libitum* throughout all experiments.

Diets and chemical induction of MASH fibrosis.

Eight to ten weeks old male or female mice were fed a normal chow diet, the obesogenic Gubra-Amylin NASH (GAN) diet (D09100310, Research diets, Inc)) with additional fructose (23.1g/L D-fructose (Sigma-Aldrich, F0127) and glucose (18.9g/L D-glucose (Sigma-Aldrich, G8270) supplemented in drinking water for 22 to 26 weeks or the Choline Deficient L-Amino Acid defined high-fat diet (CDAA-HFD) (A16092003, Research Diets, Inc) for 8 to 12 weeks. In some experiments, mice were subjected to chemical induction of liver fibrosis using carbon tetrachloride (CCl_4) intraperitoneal injection (Sigma-Aldrich 1:10 v/v diluted in olive oil at 2µl/g body weight) three times a week for 4 weeks. Control mice were injected with olive oil, and all animals were sacrificed 48 hours after the final injection of CCl_4. At the end of each experiment, animals were sacrificed by isoflurane (Fluriso, USP) inhalation, blood and livers were harvested for subsequent analysis.

Immunofluorescence analysis of human MASH liver

Paraffin-embedded sections of human liver were deparaffinized, rehydrated, and treated for 20 min with boiling citrate antigen retrieval buffer (Sigma-Aldrich). Slides were blocked with 5% donkey serum in 1x Tris-buffered-saline containing 0.1% Triton-X-100 (TBS-T) for 1h at room temperature and incubated overnight at 4 °C with goat anti-EphB2 (AF467, R&D System), rabbit anti-phosphoEphB1/B2$^{Y594 + Y596}$ (Abcam), and mouse anti-αSMA (1:200 dilution in 1% BSA TBS-T) antibodies. Slides were washed and incubated for 1 h with donkey anti-mouse IgG NorthernLights-493, donkey anti-rabbit or donkey anti-goat IgG Northernlghts-557 (1:500 dilution in 1% BSA-TBST). Slides were washed three times with 1xTBS-T and mounted with VECTASHIELD Antifade Mounting Medium with DAPI (VectorLabs). Images were acquired using a Nikon A1R confocal microscope and analyzed using the ImageJ software (NIH).

Immunohistochemistry

Immunohistochemistry staining was performed in 6-µm thick tissue sections. After deparaffinization and rehydration in ethanol solutions, antigen retrieval was performed in citrate buffer solution (pH 6.0) for 30 minutes at 95ºC. Endogenous peroxidase activity was blocked using hydrogen peroxide solution at room temperature, followed by washing in phosphate-buffered solution saline (PBS) and passage through distilled water. The slides were incubated overnight with rabbit anti-phosphoEphB1/B2$^{Y594 + Y596}$ antibody diluted (1:50) in 5% BSA-TBST. Slides were washed three time in TBS-T and incubated with the secondary antibody EnvisionTM Flex/HRP (with Streptavidin Peroxidase Solution, Agilent, DAKO) at 37ºC for 1 hour. Slides were stained with 3, 30-diaminobenzidine tetrahydrochloride (DAB-Agilent, DAKO), counterstained with Harris hematoxylin (Thermo Scientific™), and mounted with a resinous mounting medium (Permount™) dissolved in xylene. High power images were acquired using an EVOS M5000 widefield microscope (ThermoFisher).

Single cell preparation of liver tissue for flow cytometry

After mice were euthanized using isoflurane, blood was collected by cardiac puncture, the abdomen was exposed and the liver collected, rinse with PBS and weighed. Liver was subsequently transferred in approximately 3ml of serum-free RPMI-1640 containing Collagenase D (10mg/ml; Sigma) and DNase (1mg/ml; Sigma) and incubated in a rocking platform for 45 min at 37°C. The liver extract was mashed through a 70µm filter, the cell re-suspended in RPMI-1640 containing 10% FBS and centrifuged at 1600 rpm for 5 min. The supernatant was discarded, and the pellet re-suspended in approximately 4 ml of 70% Percoll, then transferred in 15 ml conical tube, carefully overlay with 4 ml of 30% Percoll and centrifuged 1600 rpm for 25 min with the brake turned off. The non-parenchymal cells suspension from the Percoll interface were removed and mixed with 10 mL of RPMI-1640 containing 10% FBS and the cells were centrifuged at 1600 rpm for 5 min. Red blood cells (RBC) were removed from the pelleted single cell suspensions of livers non-parenchymal cells by incubation in an ammonium chloride -based 1x RBC lysis buffer (Thermofisher, eBioscience). The cells were again pelleted and mixed with FACS buffer (2% BSA, 2mM EDTA in PBS), then stained with Zombie-NIR viability dye (BioLegend) per manufacturer's instructions to discriminate live vs

dead cells. To prevent non-specific Fc binding, the cells were incubated with Fc Block (anti-mouse CD16/32, clone 93, Biolegend) for 15 min followed by the indicated antibodies cocktail for 60 min in the dark on ice: CD45 (FITC, clone S18009F, Biolegend), CD11b (BVC421, clone M1/70, Biolegend), F4/80 (APC, clone BM8, Biolegend), TIM4 (PerCP/Cy5.5, clone RMT4-54, Biolegend), Ly6C (PE, clone HK1.4, Biolegend), MHCII (BV605, clone M5/114.15.2, Biolegend), CD11c (BV785, clone N418, Biolegend) and Ly6G (PE/Cy7, clone 1A8, Biolegend). After surface staining, cells were fixed with a paraformaldehyde-based fixation buffer (BioLegend). Flow cytometric acquisition was performed on a BD Fortessa X20 flow cytometer (BD Biosciences) and data analyzed using FlowJo software (Version 10.8.1; Tree Star Inc).

Histology

Livers specimens were fixed in 10% buffered formalin and multiple paraffin-embedded 6µm sections were stained with *H&E* Masson's Trichrome and Sirius red according to standard protocols. Images were taken at ten randomly selected field using an EVOS M5000 widefield microscope and analyzed using the ImageJ software (NIH).

Hydroxyproline measurement

Hepatic collagen content was measured using the hydroxyproline assay as previously described (Reddy & Enwemeka, 1996).

Mouse plasma collection and analysis

Blood obtained by cardiac puncture was transferred in Eppendorf tubes containing 50µl of heparin, centrifuged at room temperature for 30 min at 10000 rpm and plasma collected from the supernatant fraction. Plasma samples were snap frozen and stored at -80ºC until analysis. Plasma samples were processed in a single batch for determination of alanine aminotransferase (ALT), aspartate aminotransferase (AST) cholesterol and triglyceride levels using a DC Element chemistry analyser (HESKA).

Primary human hepatic Stellate cells.

Primary human hepatic stellate cells (HSCs) were purchased from ScienCell Research Laboratories (Carlsbad, CA, USA, catalog number 5300) and cultured in a specialty medium (ScienCell #530). LX2 cell lines were purchased from Sigma-Aldrich and cultured in the fibroblast growth kit-low serum (ATCC, VA, catalog number PCS-201-041) constituted with the following ingredients: Fibroblast basal medium, ascorbic acid, fetal bovine serum, rhFGF-basic, L-glutamine, and hydrocortisone. These cells were maintained at 37°C in a humidified 5% CO_2 incubator and medium were changed every 48 hours. HSCs between passage 1 and 3 were used in this study.

TGF-β stimulation of HSCs

HSCs were plated in 24-well tissue culture plates and cultured as described above until at least 70% confluency was reached. Subsequently, HSCs were serum-starved overnight in Dulbecco's Modified Eagle Medium/F12 (DMEM/F12) containing 0.5% Bovine Serum Albumin (BSA) and exposed to recombinant human TGF-β1, TGF-β2, and TGF-β3 all at 10 ng/ml (R&D Systems) for 3h, 6h, 12h, 24h, and 48h. At each time point, vehicle and TGF-β stimulated HSCs were used for assessment of *EPHB2* and *ACTA2*/αSMA mRNA and proteins levels by RT-qPCR or western blot.

Inhibition of canonical TGF-β/SMAD pathway.

To assess the effect of TGF-β/SMAD canonical pathway on EphB2 expression, HSCs were incubated with the TGF-β type I receptor (TβRI) inhibitors SD208 (1µM), SB525334 (200nM), and the SMAD3 inhibitor SIS3 (5µM) (all from Tocris) for 4h before stimulation with recombinant human TGF-β1 (10ng/ml) for 48h. RNA was extracted to assess *EPHB2* mRNA expression by RT-qPCR.

siRNA transfections of HSCs

HSCs (70% confluency) were transfected with *EPHB2,* SMAD2, and *SMAD3* Mission®-esiRNA (Sigma Aldrich, USA) delivered into the cells using the lipofectamine® RNAiMAX (Invitrogen, USA) reagent according to the manufacturer's instruction. Mission®-esiRNA complexes targeting eGFP were used as non-targeting control. After 48H incubation, transfected HSCs were stimulated with recombinant human TGF-β1 at 10 ng/ml for another 48H. Cells were used for immunofluorescence staining or harvested for RNA and proteins extractions.

RNA extraction, cDNA synthesis and qPCR

Total RNA was extracted using RNA Stat60® (Tel-Test Inc, USA) following standard phenol-chloroform procedure, and further purified using the NucleoSpin RNA-II purification kit (Machery-Nagel) following the manufacturer's instructions. Complementary DNAs were generated by reverse transcription using Superscript reverse transcriptase-II (Invitrogen, USA) as previously described (Mimche et al., 2018). Real-time qPCR reactions were performed using Quantitect SYBR Green PCR reagent (Qiagen) and qPCR reaction plates run in the Applied BioSystems FAST 7000 Sequence detection system (ABI Prism FAST 7000). Primer sequences are shown in Supplementary Table 1 and 2, and were designed using the web-based application PrimerBank (Wang et al., 2012). Transcripts were normalized to different housekeeping genes, *glyceraldehyde-3-phosphate dehydrogenase* (GAPDH) and *hypoxanthine-guanine phosphoribosyl transferase* (*HPRT*). Messenger RNA expression levels were calculated using the $2^{-\Delta\Delta Ct}$ method.

EPHB2 locus-specific Chromatin Immunoprecipitation

HSCs were serum-starved overnight and then treated with rhTGF-β1 at 5 ng/ml for 3 hours. Control cells were not treated. Cells were then harvested for the ChIP assay using the ChIP-IT High Sensitivity kit (Cat 53040, Active Motif) as per the manufacturer's recommendation. Briefly, proteins were cross-linked to DNA in living cells with formaldehyde, cells were lysed, homogenized with a chilled Dounce homogenizer to release nuclei. The nuclear pellet was resuspended in sonication buffer and shared on ice using a digital sonicator (Branson SFX 150, EMERSON) at amplitude setting of 40% with pulse rate 30 seconds on and 30 seconds off to yield DNA fragment sizes of 200 - 1200 bp. The shared chromatin (~30 µg) samples were immunoprecipitated using 4µg of SMAD3 antibodies (Abcam, ab28379) or purified anti-human IgG Fc (Cat 410701, BioLegend) overnight at 4□C. The immune complexes were collected by incubation with Protein G Agarose beads (Cat 37499, Active Motif), followed by reverse crosslinking, digestion with Proteinase K and DNA purification. Enrichment of *EPHB2* promoter sequences in the immunoprecipitated eluted DNA was determined by qPCR using the set of primers designed based on the estimated binding region of EPHB2 (Table S1).

Immunofluorescence of HSCs

HSCs controls and HSCs-transfected with *siEPHB2* were seeded on chamber slides, treated with vehicle or TGF-β1 as described above and fixed with 4% PFA for 10–15 min. The cells were then washed three times with TBS-T, blocked for one hour in blocking solution (5% donkey serum; 0.1% triton-X-100 in TBS) and incubated overnight at 4 °C with a primary antibody against EPHB2 (AF467, R&D System), and α-SMA (clone 1A4, R&D system; 1:200 in blocking solution). The next day, samples were washed three times with TBS-T incubated for one hour with donkey anti-goat IgG NorthernLights-493 and donkey anti-mouse IgG, NorthernLights-557 (1:500) (R&D System) in blocking solution. Samples were washed three times with TBS-T and mounted with VECTASHIELD Antifade Mounting Medium with DAPI (Vectorlabs). Images were acquired with a Nikon A1R confocal microscope.

RNA sequencing

RNA sequencing was performed as prevoiuosly described (Egal et al 2014) Total RNA from EphB2-knockout and control HSCs stimulated with rhTGF-β1 were extracted as described above. RNA sequencing was performed by Novogene on an Illumina NovaSeq platform using a paired-end 150-bp sequencing strategy. The human GRCh38 and mouse GRCm38 genome and gene annotation files were downloaded from Ensembl release 98 and a reference database was created using STAR version 2.7.2c with splice junctions optimized for 150 base pair reads (Dobin et al., 2013). Optical duplicates were removed from the paired end FASTQ files using clumpify v38.34 and reads were trimmed of adapters using cutadapt 1.16 (Kechin et al., 2017). The trimmed reads were aligned to the reference database using STAR in two pass mode to output a BAM file sorted by coordinates. Mapped reads were assigned to annotated genes

using featureCounts version 1.6.3 (Liao et al., 2014). The output files from cutadapt, FastQC, FastQ Screen, Picard CollectRnaSeqMetrics, STAR and featureCounts were summarized using MultiQC to check for any sample outliers (Ewels et al., 2016). Differentially expressed genes were identified using a 5% false discovery rate with DESeq2 version 1.26.0 (Love et al., 2014). Pathways were analyzed using the fast gene set enrichment package and Ingenuity Pathway Analysis (Krämer et al., 2014) (Qiagen, Inc). The RNA-seq datasets have been deposited in the GEO database (GSE274897, GSE274898, GSE274899).

Immunoprecipitation & Immunoblotting

Samples were lysed in radioimmunoprecipitation assay (RIPA) buffer supplemented with protease and phosphatase inhibitors (Thermo Scientific). Protein concentrations were determined using Pierce Rapid Gold BCA protein Assay Kit (Thermo Scientific), diluted to a concentration of 2,000µg/ml of protein. EphB2 proteins were immunoprecipitated using the Dynabeads Protein A Immunoprecipitation kit (Invitrogen) with 2µg of anti-EphB2 antibody (R&D Systems, AF467), heated for 15 mins at 70°C and cooled down on ice. Subsequently, proteins were separated by SDS–PAGE electrophoresis and transferred to 0.2µm PVDF membranes (Millipore, Merck). Membranes were incubated in blocking solution (1% gelatin in 1X TBS with 0.5% Tween 20, Sigma) for 1.5 hour, and primary antibody was incubated overnight at 4°C in the blocking solution. The antibodies and their concentrations are the following: anti-EPHB2 (R&D Systems, AF467, 1:2,000), and anti-TGFβR2 (E5M6F, 1:1000, CST-41896, Cell Signaling Technology) Following several washes in TBST (TBS with 0.5% Tween 20), horseradish peroxidase (HRP)-labeled secondary antibodies (1:5,000) were incubated for 1 h at room temperature in 10% nonfat dry milk TBST. Membranes were developed with the Super Signal West Pico PLUS Chemiluminescent western-blotting substrate (Thermo Scientific).

Western blot

Cells were lysed in ice-cold RIPA buffer containing protease and phosphatase inhibitor cocktails (Thermo Fisher Scientific). Protein concentration in cell lysates were determined using a Pierce™ rapid gold bicinchoninic acid (BCA) protein assay kit from ThermoFisher Scientific. Proteins were loaded and resolved on a 10% Tris-Glycine SDS-PAGE gels, electro-transferred onto nitrocellulose membrane and incubated overnight at 4°C with specific antibodies. These antibodies and their concentrations are the following: anti-EPHB2 (R&D Systems, AF467, 1:2,000), anti-α-SMA (D4K9N, 1:10,000), anti-phospho-SMAD2/3 (D27F4, 1:10,000) anti-SMAD2/3, (D7G7, 1:1000), anti-phospho-AKT (D9E, 1:1000), anti-AKT (40D4, 1:10,000) anti-SMURF2 (D8B8, 1:1000) and anti-vinculin (E1E9V; 1:10,000) all from Cell Signaling Technology. Immunoreactivity was revealed by incubation with host-specific secondary antibodies conjugated with horseradish peroxidase, followed by detection with SuperSignal West Pico Chemiluminescent Substrate from ThermoFisher. Images were acquired using an Amersham imager 680 Chemi system from GE Healthcare.

Kinome array and analysis

PamGene's KinomePro approach measure the ability of active kinases in a cell lysate sample to phosphorylate specific peptides imprinted on PamChip® microarray (Hilhorst et al., 2009). The PamChip® consists of 4 identical arrays, each array containing 144 (STK) or 196 (PTK) phosphosites. HSCs (70% confluency) were transfected with *EPHB2* Mission®-esiRNA (Sigma Aldrich, USA) delivered into the cells using the lipofectamine® RNAiMAX (Invitrogen, USA) reagent according to the manufacturer's instruction. Mission®-esiRNA complexes targeting eGFP were used as non-targeting control. After 48H incubation, transfected HSCs were further stimulated with recombinant human TGF-β1 at 10 ng/ml for 48H. Whole-cell lysates were prepared according to PamGene instructions. PamChip PTK and STK arrays were performed by PamGene. Measurements of kinome activity were performed on a PamStation-12 by PamGene (Chirumamilla et al., 2019). Briefly, the PamChip PTK array was processed in a single-step reaction in which 5.0 microgram of protein lysate was dispensed onto PTK array dissolved in protein kinase buffer (PamGene proprietary information) and additives including 1% BSA, 10 mmol/L dithiothreitol, FITC conjugated pY20 antibody, and 400 mmol/L ATP. The STK array was processed in a two-step reaction in which 1.5 microgram of protein lysate was used with protein kinase buffer (PamGene proprietary information) supplied with 1% BSA, primary STK antibody mix, and 400 mmol/L ATP (sample mix). After an initial incubation of 110 minutes, the reaction mix was removed, and the secondary FITC-labeled antibody mix was added. In both arrays, software-based image analysis (BioNavigator software V.6.3 from PamGene) integrates the signals obtained within the time course of the incubation of the kinase lysate on the chip into one single value for each peptide for each sample (exposure time scaling). Peptide phosphorylation kinetics (for PTK) and its variations (for PTK/ STK) were used to remove low signal peptides as quality control analysis (QC). Individual peptide phosphorylation intensities were log2 transformed. The peptides with significant differences in phosphorylation intensity (HSCs-*EPHB2*-silenced vs HSCs, using test, $P < 0.05$) are visualized as either volcano and bar plots or as heatmap using the R heatmap package.

Upstream kinase analysis (UKA) of PTK and STK data was done using default setting of the PamApp (PTK or STK UKA 2018 V.4.0) on BioNavigator Analysis software tool as described before (Alack et al., 2020). The analysis is based on documented kinase–substrate relationships (from iviv database and literature-based protein modifications such as HPRD, PhosphoELM, PhosphositePLUS, Reactome, UNIPROT) complemented with "in silico" predictions that are retrieved from the phosphoNET database. The analysis generated three major parameters calculated by the PamApp: (i) Median kinase statistic (MKS) depicts the overall change of the peptide set that represents a kinase. For instance, a larger positive value indicates a larger activity in treated cells compared with controls. (ii) Mean significance score (MSiS) indicating the significance of the change represented by the mean kinase statistic (s) between two groups (using 500 permutations across sample labels). (iii) Mean specificity score (MSpS) indicates the specificity of the mean kinase statistics with respect to the number of peptides used for predicting the corresponding kinase (using 500 permutations

across target peptides). The final ranking of the kinases was based on Median Final Score (MFS), which was calculated by addition of MSiS and MSpS. Top predicted kinases from significant (MFS>1.3) PTK and STK peptide sets are represented on phylogenetic tree of the human protein kinase family generated by Coral (http://phanstiel-lab.med.unc.edu/CORAL/; ref. 30).

Migration assay

We devised a custom void filling migration assay like the migration assays provided by Ibidi (GmbH). A rectangular silicone membrane (1mm thickness, 5 mm x 15 mm) was placed in a 6-well plate, and primary human HSCs were plated around the silicone membrane at cell density approximately 50% confluence. HSCs (80% confluency) were transfected with *EPHB2* Mission®-esiRNA (Sigma Aldrich, USA) delivered into the cells using the lipofectamine® RNAiMAX (Invitrogen, USA) according to the manufacturer's instruction. Mission®-esiRNA complexes targeting eGFP were used as non-targeting control. After 48 hours upon confirming 100% confluence, silicone membrane was removed, and void was created (Time 0 hour). Cell migration was monitored every 6 hours, and images were taken at the consistent locations by referencing a marking line etched at the edge of silicone membrane. Average migratory distance was calculated from 5 different locations.

TGFβ reporter assay

The SBE reporter kits (79806 and 79578, BPS Biosciences) were used to monitor the activity of the TGFβ/SMAD signaling pathway in human HSCs, following the manufacturer's instruction. HSCs were seeded into a 24-well plate, cultured to 70- 80% confluency and transfected with *EPHB2* Mission®-esiRNA (Sigma Aldrich, USA) delivered into the cells using the lipofectamine® RNAiMAX (Invitrogen, USA) according to the manufacturer's instruction. Mission®-esiRNA complexes targeting eGFP were used as non-targeting control. After 48H, transfected HSCs were transduced with SBE luciferase reporter lentivirus and negative control luciferase lentivirus for another 24H. Next, HSCs were stimulated with recombinant human TGF-β1 at 10 ng/ml for 3H and the activation of the TGFβ/SMAD signaling pathway was monitored by measuring luciferase activity using the ONE-GLO luciferase assay system (E6110, Promega) and a luminometer (SpectraMAX iD3 plate reader), following the manufacturer's instruction. The luciferase activity from the SBE reporter was calculated by subtracting the luminescence from the negative control reporter as a background.

In situ proximity ligation assay

Cells were fixed with 4% paraformaldehyde (Biolegend)) for 15 min and permeabilized for 10 min at room temperature with 0.1% Triton-X 100 (Sigma). The following primaries antibodies were incubated overnight at 4ºC: anti-EphB2 (Goat antibody AF467, R&D Systems) and anti-TGFβR2 (Rabbit antibody, clone E5M6F, CST-41896, Cell Signaling Technology). *In situ* proximity ligation assays were performed using the Duolink In Situ reagents (Sigma). Incubation of antibodies, ligation of oligodeoxynucleotides and

amplification were performed according to the manufacturer's instructions. Nuclei were labelled with DAPI and images acquired with a Nikon A1R confocal microscope.

snRNA-seq data processing

All count matrices and metadata for each sample are publicly available in the Gene Expression Omnibus (www.ncbi.nlm.nih.gov/geo/) under data accession no. GSE212837 (Wang et al., 2023). Briefly, Cellranger count pipeline was applied to the FASTQs to perform alignment against modified transcriptomes based on the mm10 reference builds for mice that contain introns to increase mapping efficiency, and the number of genes detected. Filtered feature-barcode matrices from Cell Ranger were subsequently run through a standard Seurat pipeline for QC. Different QC parameters were used for snRNA-seq data generated using Chromium 3′ Gene Expression V2 Kits using Seurat. For snRNA-seq generated from mouse samples, we included nuclei that fit the following criteria: (i) total number of expressed genes greater than 300 and less than 6000, (ii) <5% of which annotated as mitochondrial, and (iii) total counts greater than 500 and less than 15000. Feature plots were generated using default parameters in Seurat.

Statistics

Statistical analysis and plotting were done using GraphPad Prism software 9.0.2. Comparisons between more than 2 groups were performed using Kruskal-Wallis One-Way ANOVA and the non-parametric Mann Whitney-U test was used for comparison between 2 nonrelated groups. Number of biological replicates are indicated in figure legends. Data were presented as Mean ± SEM for experiments, and p values less than 0.05 were considered significant.

Acknowledgments

We appreciate the University of Utah and Indiana University cores facilities for assistance with histology, RNA sequencing, confocal microscopy, metabolic phenotyping and flow cytometry studies. We thank Quinian Johanson for excellent animal husbandry, Erika Egal for assistance with histology, and Scott Friedman for providing reagents and resources.

Funding

Funding was provided by the NIH through the grants R21 DK115991 (to P.N.M), R01 DK128819 (to P.N.M.), and R01 AR076489 to P.N.M.

Author Contributions

P.N.M. conceived the project with input from M.H. Experiments were designed by P.N.M and M.Y., and conducted by M.Y., S.D.K., E.M.K, E.A., S.P., F.S., K.J.E., M.N.H., M.G., J.S., H.C.R., S.B., M.K. Early work, animal models, and various collections by F.S. and M.H. Results were analyzed by P.N.M., M.Y., S.D.K., M.G., J.S., H.C.R., S.B., M.K. Figures were designed by P.N.M. Analysis and visualization of single nucleus RNA sequencing data was performed by S.W. The manuscript was written by P.N.M., with subsequent editing by M.N.H., and M.H.

Competing interests

Nothing to declare

Resource availability

Lead contact

Further information and requests for resources and reagents should be directed to Lead Contact, Patrice N. Mimche (email: pmimche@iu.edu).

Figures legends

Figure 1: EphB2 deficiency dampens diet-induced MASH fibrosis in mice. (**A**) Representative images of liver sections of *Ephb2*+/+ and *Ephb2-/-* mice fed the GAN diet for 26 weeks stained with *H&E* and Masson Trichrome. (**B**) Plasma levels of liver damage enzymes ALT and AST of *Ephb2*+/+ and *Ephb2-/-* mice fed the GAN diet for 26 weeks (n = 4 mice/group, *p < 0.05, **p < 0.01 by Student's t test). (**C**) Plasma level of cholesterol and triglyceride from *Ephb2*+/+ and *Ephb2-/-* mice fed the GAN diet for 26 weeks (n = 4 mice/group, *p < 0.05, **p < 0.01 by Student's t test). (**D**) Heatmap depicting the top 40 differentially expressed genes from bulk RNA sequencing of livers samples of *Ephb2*+/+ and *Ephb2-/-* mice fed the GAN diet for 26 weeks. (**E**) Gene ontology analysis of the top significantly downregulated or upregulated pathways in RNA sequencing data in **D**. (**F**) Liver mRNA levels of fibrotic markers *Col1a1, Timp1, Edn1, Acta2, Pdgfrβ*, *Vim* and (**G**) inflammatory markers, *Cd11b, Il-6, Tnf-α, Ccr2, Tgf-β1*, and *Il-1β* in *Ephb2*+/+ and *Ephb2-/-* mice fed the GAN diet for 26 weeks (n = 5 mice/group, *p < 0.05, **p < 0.01 by Student's t test). (**H**) Representative images of liver sections of *Ephb2*+/+ and *Ephb2-/-* mice fed the CDAA-HFD diet for 12 weeks stained with *H&E* and Masson Trichrome. (**I**) Plasma levels of liver damage enzymes ALT and AST in *Ephb2*+/+ and *Ephb2-/-* mice fed the CDAA-HFD (n = 9-11 mice/group, *p < 0.05 by Student's t test). (**J**) Plasma level of cholesterol and triglyceride in *Ephb2*+/+ and *Ephb2-/-* mice fed the CDAA-HFD (n = 9-11 mice/group, *p < 0.05, **p < 0.01 by Student's t test. (**K**) Level of hydroxyproline quantified in the livers of *Ephb2*+/+ and *Ephb2-/-* mice fed the CDAA-HFD (n = 7-10 mice per group, *p < 0.05, **p < 0.01 by Student's t test). (**L**) Liver mRNA levels of fibrotic and inflammatory markers, *Col1a1, Col6a2, Acta2, Tgf-β1, Smad3, Il-1β, Il-6, Cd11b* in *Ephb2*+/+ and *Ephb2-/-* mice fed the CDAA-HFD for 12 weeks (n = 9-11 mice/group, *p < 0.05, **p < 0.01 by Student's t test). Data are presented as mean ± SEM, ns = not significant.

Figure 1

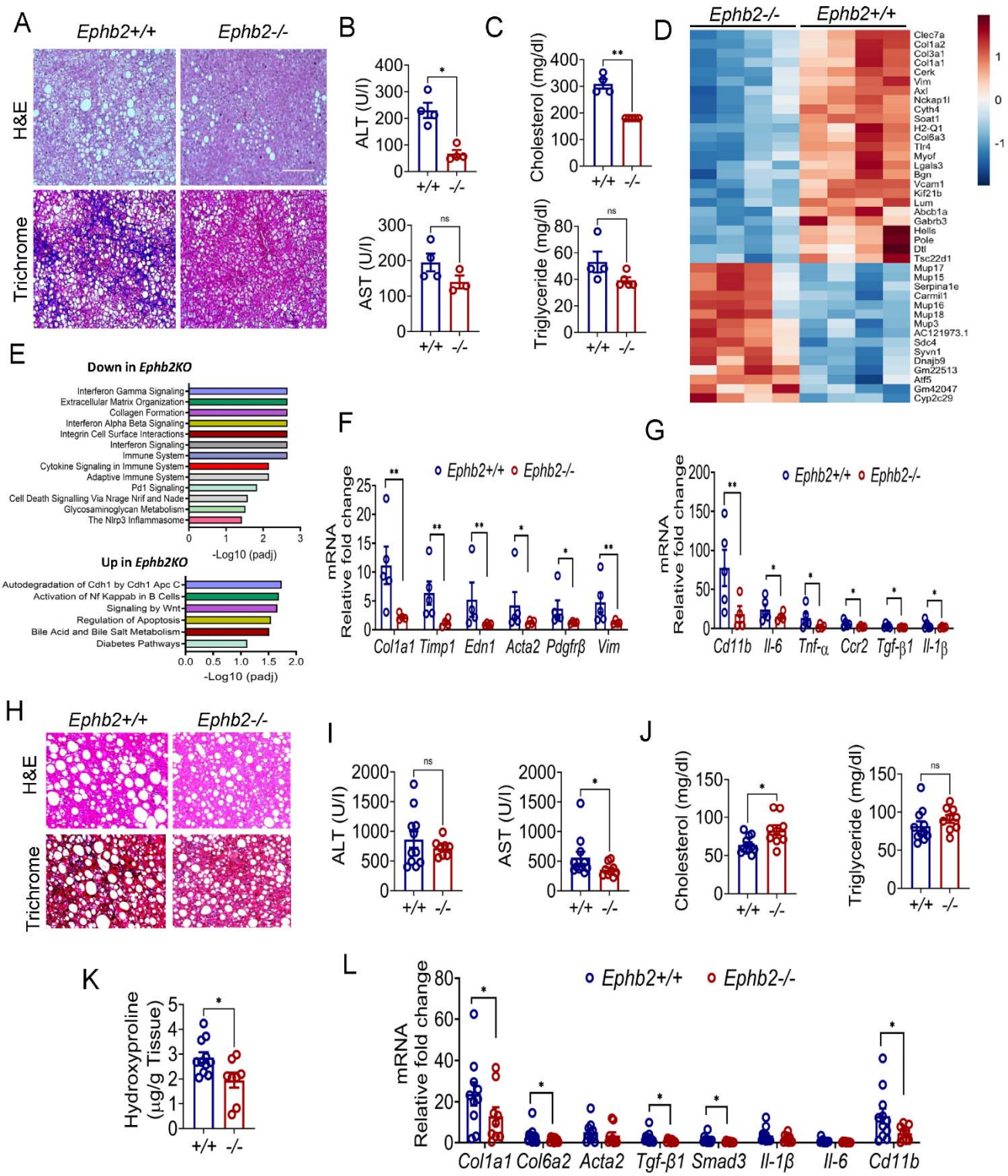
A
Ephb2+/+
Ephb2-/-
H&E
Trichrome
B
ALT (U/l)
AST (U/l)
C
Cholesterol (mg/dl)
Triglyceride (mg/dl)
D
Ephb2-/-
Ephb2+/+
Clec7a
Col1a2
Col3a1
Col1a1
Cerk
Vim
Axl
Nckap1l
Cyth4
Soat1
H2-Q1
Col6a3
Tlr4
Myof
Lgals3
Bgn
Vcam1
Kif21b
Lum
Abcb1a
Gabrb3
Hells
Pole
Dtl
Tsc22d1
Mup17
Mup15
Serpina1e
Carmil1
Mup16
Mup18
Mup3
AC121973.1
Sdc4
Syvn1
Dnajb9
Gm22513
Atf5
Gm42047
Cyp2c29
E
Down in Ephb2KO
Interferon Gamma Signaling
Extracellular Matrix Organization
Collagen Formation
Interferon Alpha Beta Signaling
Integrin Cell Surface Interactions
Interferon Signaling
Immune System
Cytokine Signaling in Immune System
Adaptive Immune System
Pd1 Signaling
Cell Death Signalling Via Nrage Nrif and Nade
Glycosaminoglycan Metabolism
The Nlrp3 Inflammasome
-Log10 (padj)
Up in Ephb2KO
Autodegradation of Cdh1 by Cdh1 Apc C
Activation of Nf Kappab in B Cells
Signaling by Wnt
Regulation of Apoptosis
Bile Acid and Bile Salt Metabolism
Diabetes Pathways
-Log10 (padj)
F
Ephb2+/+
Ephb2-/-
mRNA Relative fold change
Col1a1
Timp1
Edn1
Acta2
Pdgfrβ
Vim
G
Ephb2+/+
Ephb2-/-
mRNA Relative fold change
Cd11b
Il-6
Tnf-α
Ccr2
Tgf-β1
Il-1β
H
Ephb2+/+
Ephb2-/-
H&E
Trichrome
I
ALT (U/l)
AST (U/l)
J
Cholesterol (mg/dl)
Triglyceride (mg/dl)
K
Hydroxyproline (μg/g Tissue)
L
Ephb2+/+
Ephb2-/-
mRNA Relative fold change
Col1a1
Col6a2
Acta2
Tgf-β1
Smad3
Il-1β
Il-6
Cd11b

Figure 2: EphB2-mediated MASH fibrosis is kinase dependent. (**A**) Representative images of livers from EphB2-F620D, wild type and EphB2-K661R mice fed the GAN diet for 26 weeks photographed, and sections stained with *H&E* and Masson Trichrome. (**B**) Level of hydroxyproline quantified in the livers of EphB2-F620D, wild type and EphB2-K661R mice fed the GAN diet for 26 weeks (n = 8 mice/group). (**C**) Plasma levels of liver damage enzymes ALT and AST in EphB2-F620D, wild type and EphB2-K661R mice fed the GAN diet (n=8-11 mice/group, $^{**}p < 0.01$ by ANOVA test. (**D**) plasma level of cholesterol and triglycerides (**E**) Liver to body weight ratio of EphB2-F620D, wild type and EphB2-K661R mice fed the GAN diet (n = 8-11 mice per group, $^{*}p < 0.05$, $^{**}p < 0.01$, $^{***}p < 0.001$ by ANOVA). (**F**) Liver mRNA levels of fibrotic and inflammatory markers *Col1a1, Col3a1, Col6a2, Tgf-β1, Il-1β, Il-6, Cd11b* in EphB2-F620D, wild type and EphB2-K661R mice fed the GAN diet for 26 weeks (n = 8-11 mice/group, $^{*}p < 0.05$, $^{**}p < 0.01$, by ANOVA). (**G**) Representative images of livers section of EphB2-F620D, wild type and EphB2-K661R receiving CCl_4 for 4 weeks and stained with *H&E*, Masson Trichrome and Sirius red. (**H**) Level of hydroxyproline quantified in the livers of EphB2-F620D, wild type and EphB2-K661R mice receiving CCl_4 for 4 weeks (n = 4-5 mice/group). (**I**) Plasma levels of liver damage enzymes ALT and AST in EphB2-F620D, wild type and EphB2-K661R mice (n= 4-5 mice/group, $^{*}p < 0.05$, $^{**}p < 0.01$ by ANOVA). (**J**) Percentage of myeloid cell subsets population ($CD11b^{hi}$, cDC1, F4/80) in the liver of EphB2-F620D, wild type and EphB2-K661R mice receiving CCl_4 for 4 weeks (n= 4-5 mice/group, $^{*}p < 0.05$, $^{**}p < 0.01$, $^{****}p < 0.0001$ by ANOVA). (**K**) Liver mRNA levels of fibrotic markers *Col1a1, Col3a1, Acta2, Timp1, Col1a2,* and *Col6a2* in EphB2-F620D, wild type and EphB2-K661R mice receiving CCl_4 for 4 weeks (n = 4-5 mice/group, $^{*}p < 0.05$, $^{**}p < 0.01$ by ANOVA). Data are presented as mean ± SEM, ns = not significant.

Figure 2

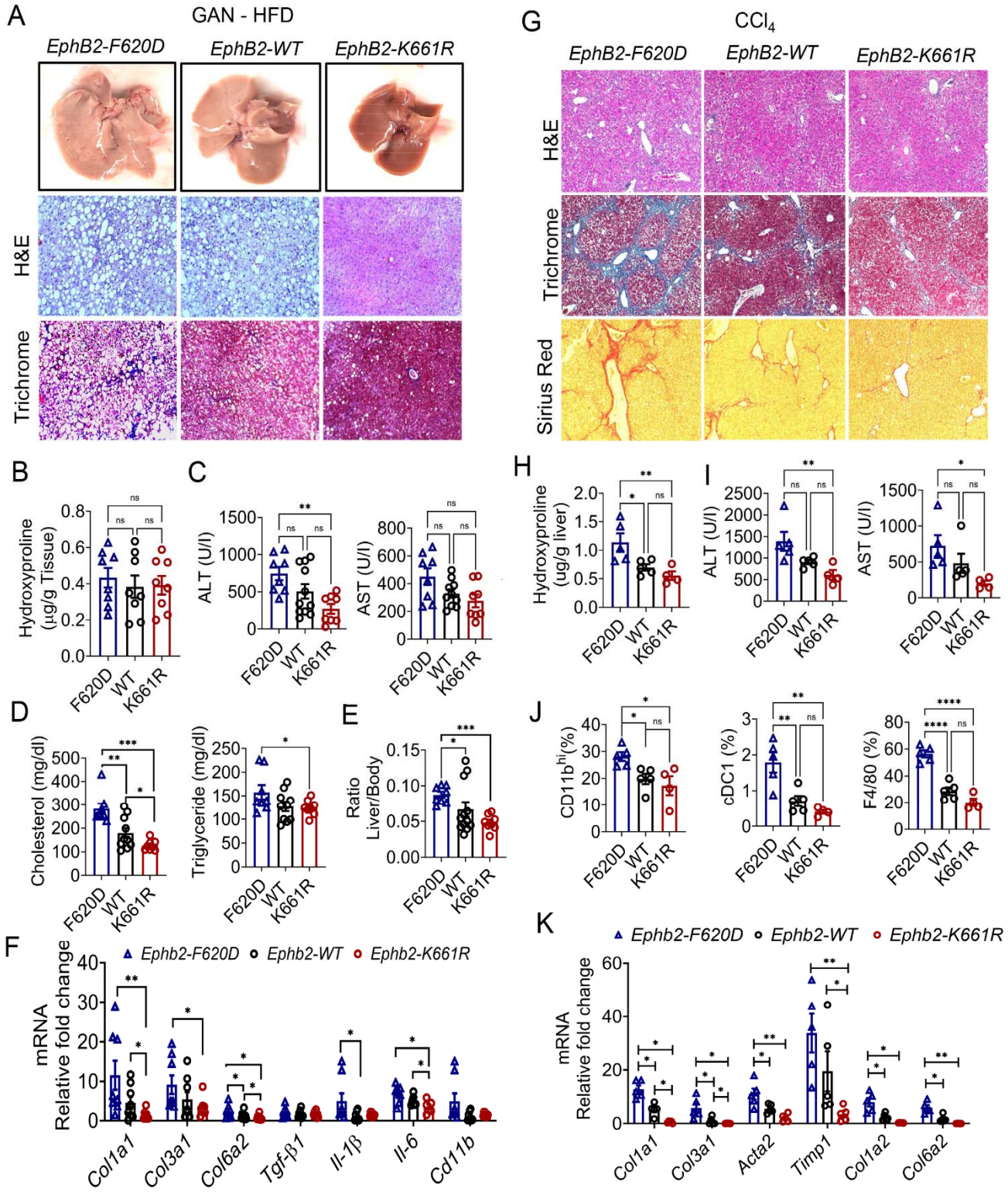
A
GAN - HFD
EphB2-F620D
EphB2-WT
EphB2-K661R
H&E
Trichrome
G
CCl4
EphB2-F620D
EphB2-WT
EphB2-K661R
H&E
Trichrome
Sirius Red
B
Hydroxyproline (µg/g Tissue)
C
ALT (U/l)
AST (U/l)
H
Hydroxyproline (ug/g liver)
I
ALT (U/l)
AST (U/l)
D
Cholesterol (mg/dl)
Triglyceride (mg/dl)
E
Ratio Liver/Body
J
CD11b^hi(%)
cDC1 (%)
F4/80 (%)
F620D
WT
K661R
F
Ephb2-F620D
Ephb2-WT
Ephb2-K661R
mRNA Relative fold change
Col1a1
Col3a1
Col6a2
Tgf-β1
Il-1β
Il-6
Cd11b
K
Ephb2-F620D
Ephb2-WT
Ephb2-K661R
mRNA Relative fold change
Col1a1
Col3a1
Acta2
Timp1
Col1a2
Col6a2

Figure 3: TGF-β/SMAD signaling induces EphB2 expression in primary human hepatic stellate cells. (**A**) Dot plot showing *Ephb2* gene expression across different hepatic cell types in mouse snRNA-seq analyzed from published dataset GSE212837. (**B**) Representative immunofluorescence images of human liver sections of healthy and MASH patients stained with antibodies against phosphoEphB2 (Red) and αSMA (green), DAPI counterstain for nuclei is shown in blue. (**C**) Messenger RNA level of *EPHB2*, *COL1A2*, and *ACTA2* in TGF-β1 stimulated primary human HSCs at various time point (n=3). (**D**) Western blot showing proteins level of EphB2, aSMA, pSmad2/3 Smad2/3 and Vinculin in TGF-β1 stimulated primary human HSCs at various time point. (**E**) Messenger RNA level of *EPHB2* upon inhibition of canonical TGF-β/SMAD with SIS3 Smad3 inhibitor, SD208 TGFβR1 inhibitor, and SB525334 TGFβR2 inhibitor in TGF-β1-treated primary human HSCs (n=5-7). **(F**) Effects of silencing Smad2 and Smad3 with Mission®-esiRNA on TGF-β-induced *EPHB2* mRNA expression in primary human HSCs (n=3). Non-targeting Mission®-esiRNA was used as control. (**G**) Accessibility peaks for the transcription factor SMAD3 on the promoter of human *EPHB2* locus identified from a publicly available ChIP-seq dataset of TGF-β1 stimulated LX2 cells (GSE38103). (**H**) Enrichment of SMAD3 binding sites on the promoter of human *EPHB2* validated by ChIP-qPCR in TGF-β1 stimulated primary human HSCs. All these data presented as mean ± SEM, *$p < 0.05$, **$p < 0.01$, ***$p < 0.001$, ****$p < 0.0001$ by ANOVA ns = not significant.

Figure 3

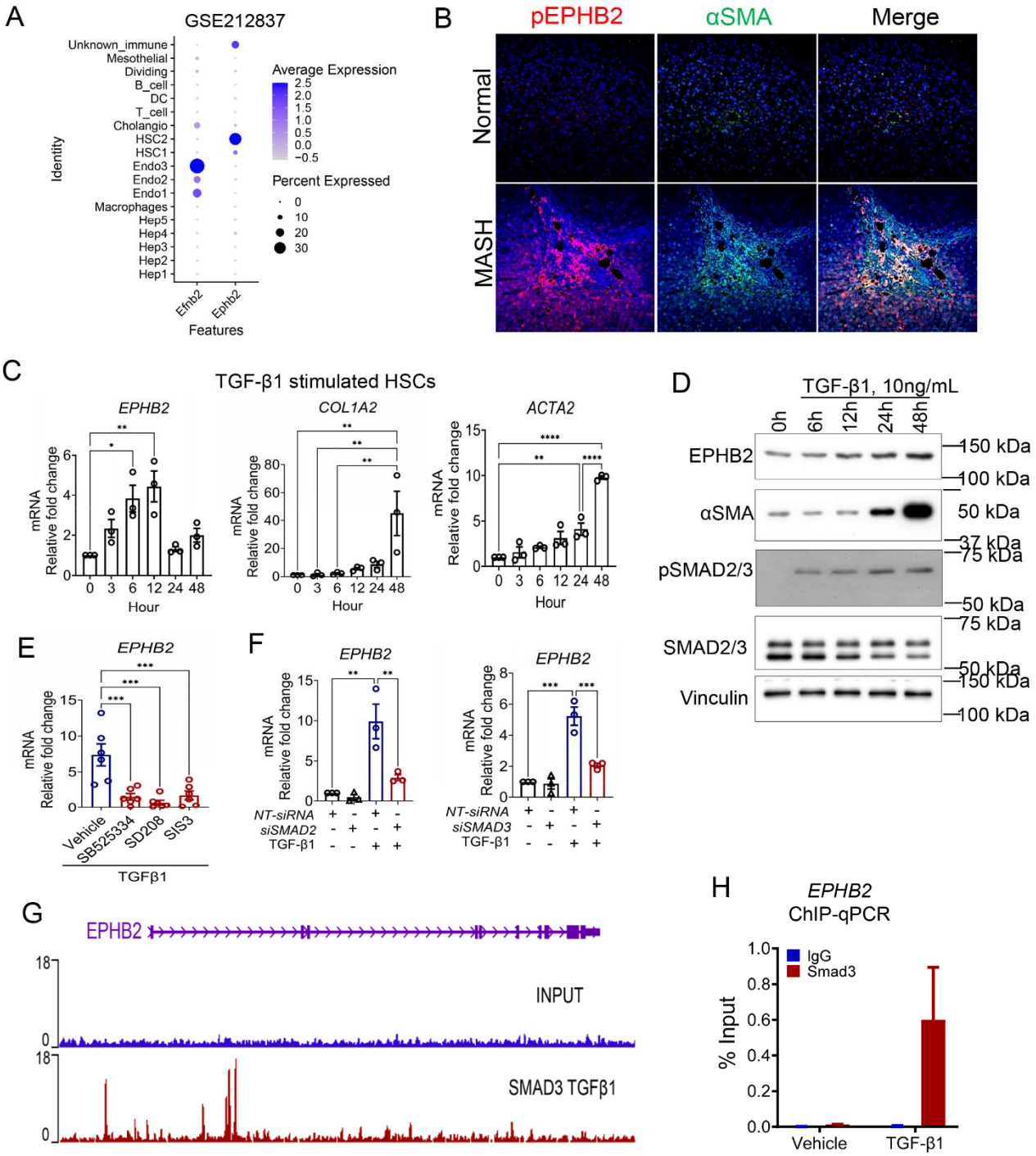
A
GSE212837
Unknown_immune
Mesothelial
Dividing
B_cell
DC
T_cell
Cholangio
HSC2
HSC1
Endo3
Endo2
Endo1
Macrophages
Hep5
Hep4
Hep3
Hep2
Hep1
Identity
Efnb2
Ephb2
Features
Average Expression
Percent Expressed
B
pEPHB2
αSMA
Merge
Normal
MASH
C
TGF-β1 stimulated HSCs
EPHB2
COL1A2
ACTA2
mRNA Relative fold change
Hour
D
TGF-β1, 10ng/mL
0h
6h
12h
24h
48h
EPHB2
αSMA
pSMAD2/3
SMAD2/3
Vinculin
150 kDa
100 kDa
50 kDa
37 kDa
75 kDa
E
Vehicle
SB525334
SD208
SIS3
TGFβ1
F
NT-siRNA
siSMAD2
siSMAD3
TGF-β1
G
EPHB2
INPUT
SMAD3 TGFβ1
H
EPHB2
ChIP-qPCR
IgG
Smad3
% Input
Vehicle
TGF-β1

Figure 4: Silencing EPHB2 abrogates TGF-β-induced HSC-to-myofibroblasts trans-differentiation. (**A**) Messenger RNA level of *EPHB2* and (**B**) *ACTA2* and *COL1A1* mRNA levels measured in different HSCs lines treated with Mission® *EPHB2*-esiRNA (SIGMA), stimulated with TGF-β1 at 10ng/ml and normalized to the same HSCs lines treated with nontargeting Mission®-esiRNA (n=5). (**C**) Representative immunofluorescence images of TGF-β1-treated HSCs transfected with *EPHB2*-siRNA and non-targeted -siRNA, stained with antibodies against EphB2 (green) and αSMA (red). (**D**) Western blot gels images showing the effects of silencing *EPHB2* with Mission®-esiRNA on TGF-β1-induced EphB2, αSMA, Smurf2, and Vinculin proteins levels in primary human HSCs for 48 hours. (**E**) Potential protein-protein interaction between EphB2 and TGFBRII detected by immunoprecipitation of EphB2 in TGF-β1 stimulated human HSCs followed by western blot of EphB2 and TGFBRII. (**F**) Proximity ligation assay data of EphB2 and TGFβRII interaction in HSCs. (**G**) Western blot gels images showing the effects of silencing *EPHB2* with Mission®-esiRNA on TGF-β1-induced EphB2, pSmad2/3, Smad2/3, pAKT-Ser473, AKT, and Vinculin proteins levels in primary human HSCs for 1 hour. (**H**) TGF-β1-stimulated EPHB2-knocked down and control HSCs were transduced with AAV8 expressing luciferase under the control of the TGFβ-SBE-promoter reporter. TGFβ-induced SMAD activation in HSCs for 3 hours was assessed by measuring luciferase activity (n=3). (**I**) Heatmap depicting the top 40 differentially expressed genes in bulk RNA sequencing of TGF-β1-stimulated HSCs lines treated with nontargeting-esiRNA and *EPHB2*-esiRNA. (**J**) Gene ontology analysis of the top significantly downregulated or upregulated pathways in RNA sequencing data in **I.** (**K**) Live cells imaging and (**L**) quantification of HSCs migration in non-targeted and *EPHB2*-esiRNA transfected HSCs lines at various time point. Data are presented as mean ± SEM, $*p < 0.05$, $**p < 0.01$ by Student's t test ns = not significant.

Figure 4

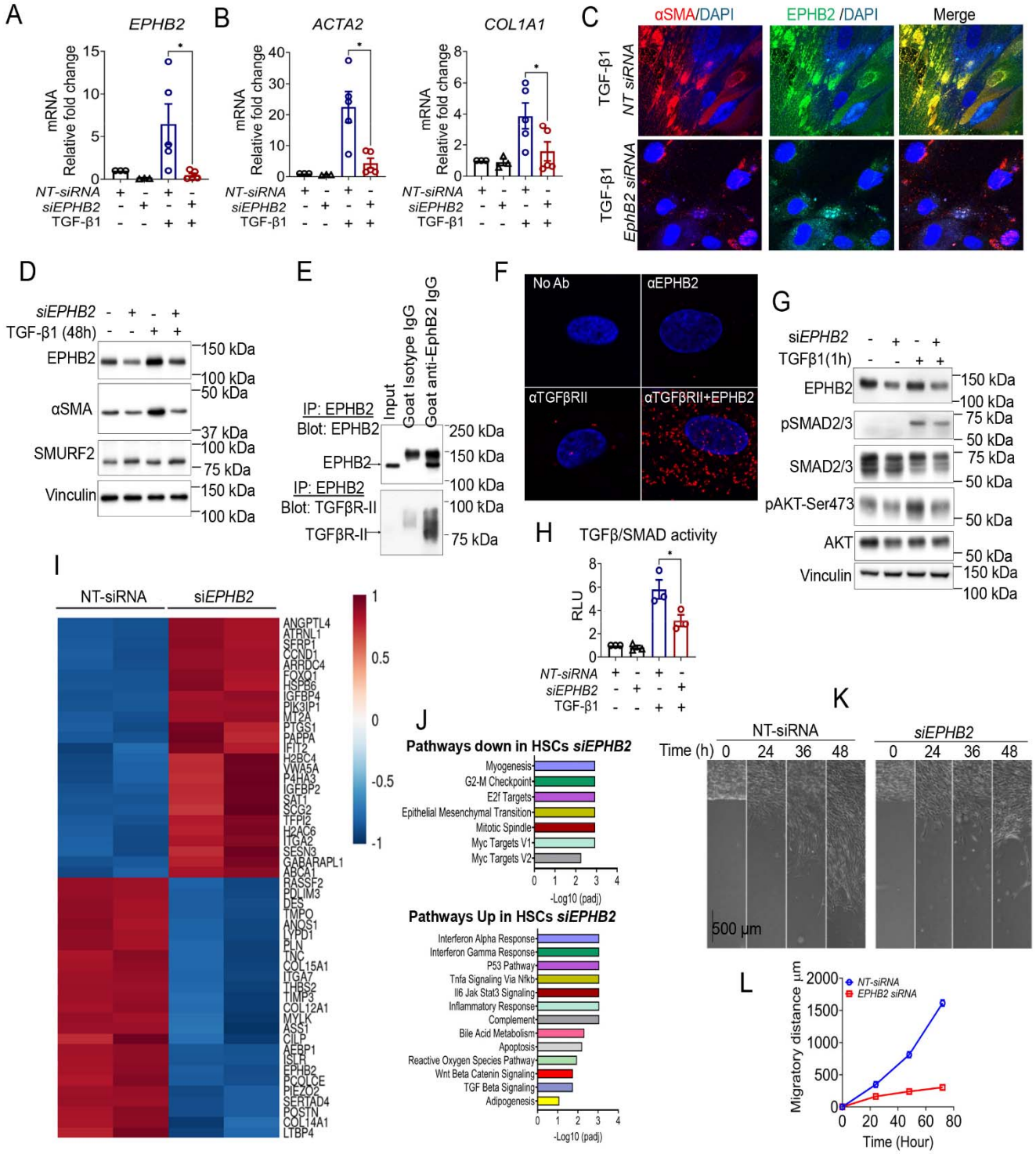
A
EPHB2
mRNA Relative fold change
NT-siRNA
siEPHB2
TGF-β1
B
ACTA2
COL1A1
C
αSMA/DAPI
EPHB2 /DAPI
Merge
TGF-β1
NT siRNA
EphB2 siRNA
D
siEPHB2
TGF-β1 (48h)
EPHB2
αSMA
SMURF2
Vinculin
150 kDa
100 kDa
50 kDa
37 kDa
75 kDa
E
Input
Goat Isotype IgG
Goat anti-EphB2 IgG
IP: EPHB2
Blot: EPHB2
IP: EPHB2
Blot: TGFβR-II
TGFβR-II
250 kDa
F
No Ab
αEPHB2
αTGFβRII
αTGFβRII+EPHB2
G
siEPHB2
TGFβ1(1h)
pSMAD2/3
SMAD2/3
pAKT-Ser473
AKT
H
TGFβ/SMAD activity
RLU
I
NT-siRNA
siEPHB2
ANGPTL4
ATRNL1
SFRP1
CCND1
ARRDC4
FOXQ1
HSPB6
IGFBP4
PIK3IP1
MT2A
PTGS1
PAPPA
IFIT2
H2BC4
VWA5A
P4HA3
IGFBP2
SAT1
SCG2
TFPI2
H2AC6
ITGA2
SESN3
GABARAPL1
ABCA1
RASSF2
PDLIM3
DES
TMPO
ANOS1
CYP01
PLN
TNC
COL15A1
ITGA7
THBS2
TIMP3
COL12A1
MYLK
ASS1
CILP
AEBP1
ISLR
EPHB2
PCOLCE
PIEZO2
SERTAD4
POSTN
COL14A1
LTBP4
J
Pathways down in HSCs siEPHB2
Myogenesis
G2-M Checkpoint
E2f Targets
Epithelial Mesenchymal Transition
Mitotic Spindle
Myc Targets V1
Myc Targets V2
-Log10 (padj)
Pathways Up in HSCs siEPHB2
Interferon Alpha Response
Interferon Gamma Response
P53 Pathway
Tnfa Signaling Via Nfkb
Il6 Jak Stat3 Signaling
Inflammatory Response
Complement
Bile Acid Metabolism
Apoptosis
Reactive Oxygen Species Pathway
Wnt Beta Catenin Signaling
TGF Beta Signaling
Adipogenesis
K
NT-siRNA
siEPHB2
Time (h)
500 μm
L
Migratory distance μm
Time (Hour)
NT-siRNA
EPHB2 siRNA

Figure 5: Deletion of *Ephb2* in hepatic stellate cells mitigates CDAA-HFD-induced MASH fibrosis. (**A**) Representative images of liver sections of *Ephb2*$^{fl/fl}$ (HSC^{WT}) and HSC$^{\Delta Ephb2}$ mice fed the CDAA-HFD for 8 weeks, stained with *H&E* and Masson-Trichrome. (**B**) Level of hydroxyproline quantified in the livers of *Ephb2*$^{fl/fl}$ (HSC^{WT}) and HSC$^{\Delta Ephb2}$ mice fed the CDAA-HFD (n = 5-7 mice/group, $^{**}p < 0.01$ by Student's t test). (**C**) Plasma levels of liver damage enzymes ALT and AST in *Ephb2*$^{fl/fl}$ (HSC^{WT}) and HSC$^{\Delta Ephb2}$ mice fed the CDAA-HFD (n=5-7 mice/group). (**D**) Plasma level of cholesterol and triglycerides in *Ephb2*$^{fl/fl}$ (HSC^{WT}) and HSC$^{\Delta Ephb2}$ mice fed the CDAA-HFD (*n* = 5-7 mice/group). (**E**) Liver mRNA levels of *Col1a1, Col3a1, Col6a2, and Acta2* in *Ephb2*$^{fl/fl}$ (HSC^{WT}) and HSC$^{\Delta Ephb2}$ mice fed the CDAA-HFD (*n* = 5-7 mice/group, $^{*}p < 0.05$, $^{**}p < 0.01$, by Student t test). (**F**) Liver mRNA levels of *Cd11b, Il-1β, and Il-6* in *Ephb2*$^{fl/fl}$ (HSC^{WT}) and HSC$^{\Delta Ephb2}$ mice fed the CDAA-HFD (*n* = 5-7 mice/group). (**G**) Heatmap depicting the top 40 differentially expressed genes from bulk RNA sequencing of livers tissues of *Ephb2*$^{fl/fl}$ (HSC^{WT}) and HSC$^{\Delta Ephb2}$ mice fed the CDAA-HFD. (**H**) Gene ontology analysis of the top significantly downregulated or upregulated pathways in RNA sequencing data in **G.** (**I**) Percentage of subsets of myeloid cells population in the livers of *Ephb2*$^{fl/fl}$ (HSC^{WT}) and HSC$^{\Delta Ephb2}$ mice fed the CDAA-HFD (n = 5-7 mice/group). Data are presented as mean ± SEM, ns = not significant.

Figure 5

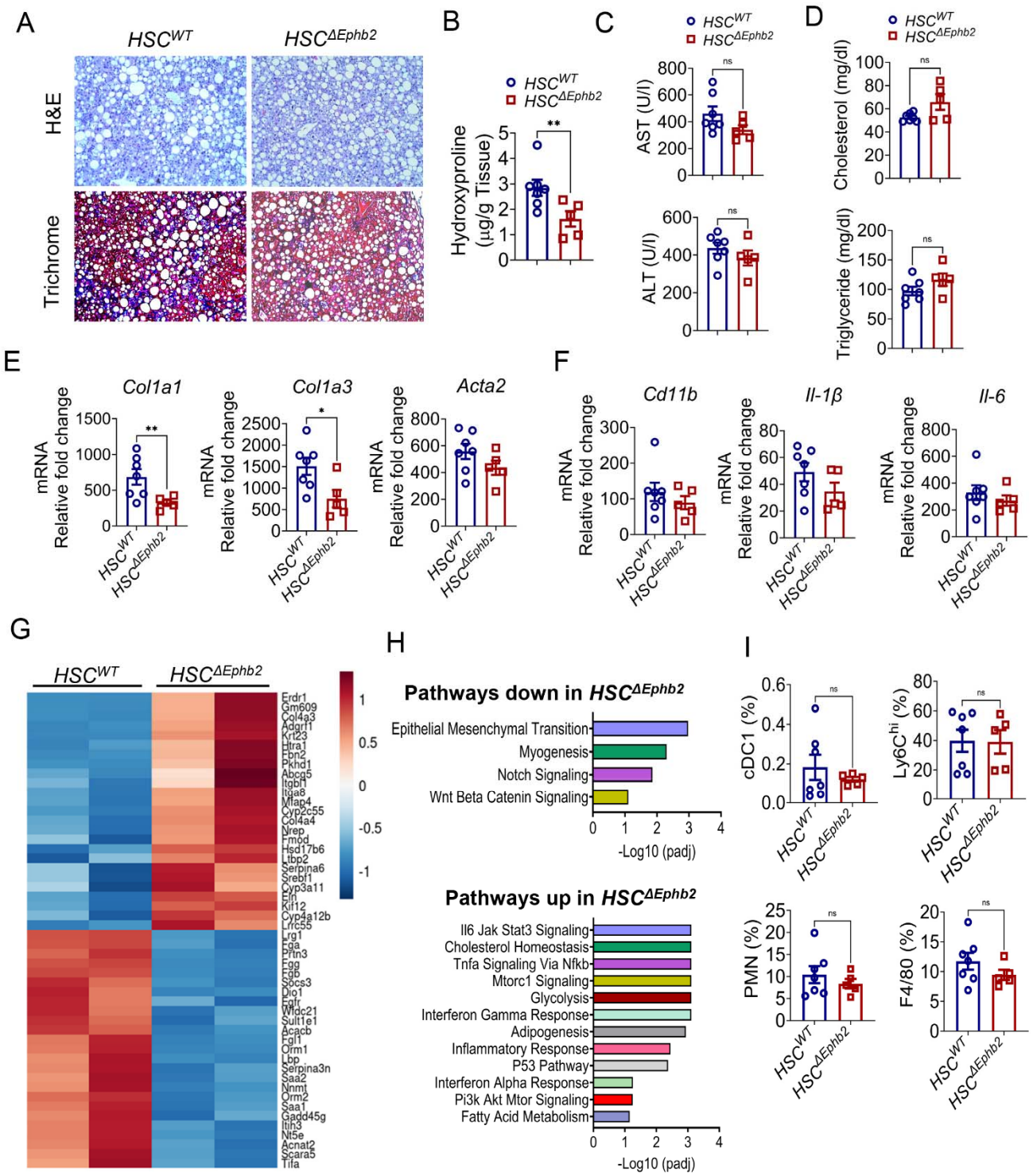

Figure 6: Deletion of *Ephb2* in hepatic stellate cells mitigates GAN diet-induced MASH fibrosis. *EphB2*$^{fl/fl}$ mice (Cre-) were crossed with the tamoxifen-inducible *Col1a2Cre*^{ERT2} mice to generate *Col1a2Cre*^{ERT2}/*Ephb2*$^{fl/fl}$ (Cre+) lines. (**A**)

Representative images of liver sections of Cre- and Cre+ mice fed the GAN diet for 26 weeks, stained with *H&E* and Masson-Trichrome. (**B**) Level of hydroxyproline quantified in the livers of Cre- and Cre+ mice fed the GAN diet (n = 5 mice/group, *$p < 0.05$ by Student's t test). (**C**) Plasma levels of liver damage enzymes ALT and AST in Cre- and Cre+ mice fed the GAN diet (n=5 mice/group). (**D**) Plasma level of cholesterol and triglycerides in Cre- and Cre+ mice fed the GAN diet for 26 weeks (n = 5 mice/group, *$p < 0.05$ by Student's t test). (**E**) liver to body weight ratio of the livers of Cre- and Cre+ mice fed the GAN diet (n = 5 mice/group). (**F**) Liver mRNA levels of *Acta2, Col1a1, Col1a2, and Timp1* in Cre- and Cre+ mice fed the GAN diet (n = 5 mice/group, *$p < 0.05$ by Student t test). (**G**) Liver mRNA levels of *Cd11b, Il-1β, IL-6 and Cxcl-10* in Cre- and Cre+ mice fed the GAN diet (n = 5 mice/group). (**H**) Immunophenotyping of macrophages subset (CD11b, Ly6C, F4/80, MHC-II) dendritic cells (cDC1) and neutrophils (PMN) in the liver of Cre- and Cre+ mice fed the GAN diet (n = 5 mice/group, *$p < 0.05$ by Student's t test). Data are presented as mean ± SEM, ns = not significant.

Figure 6

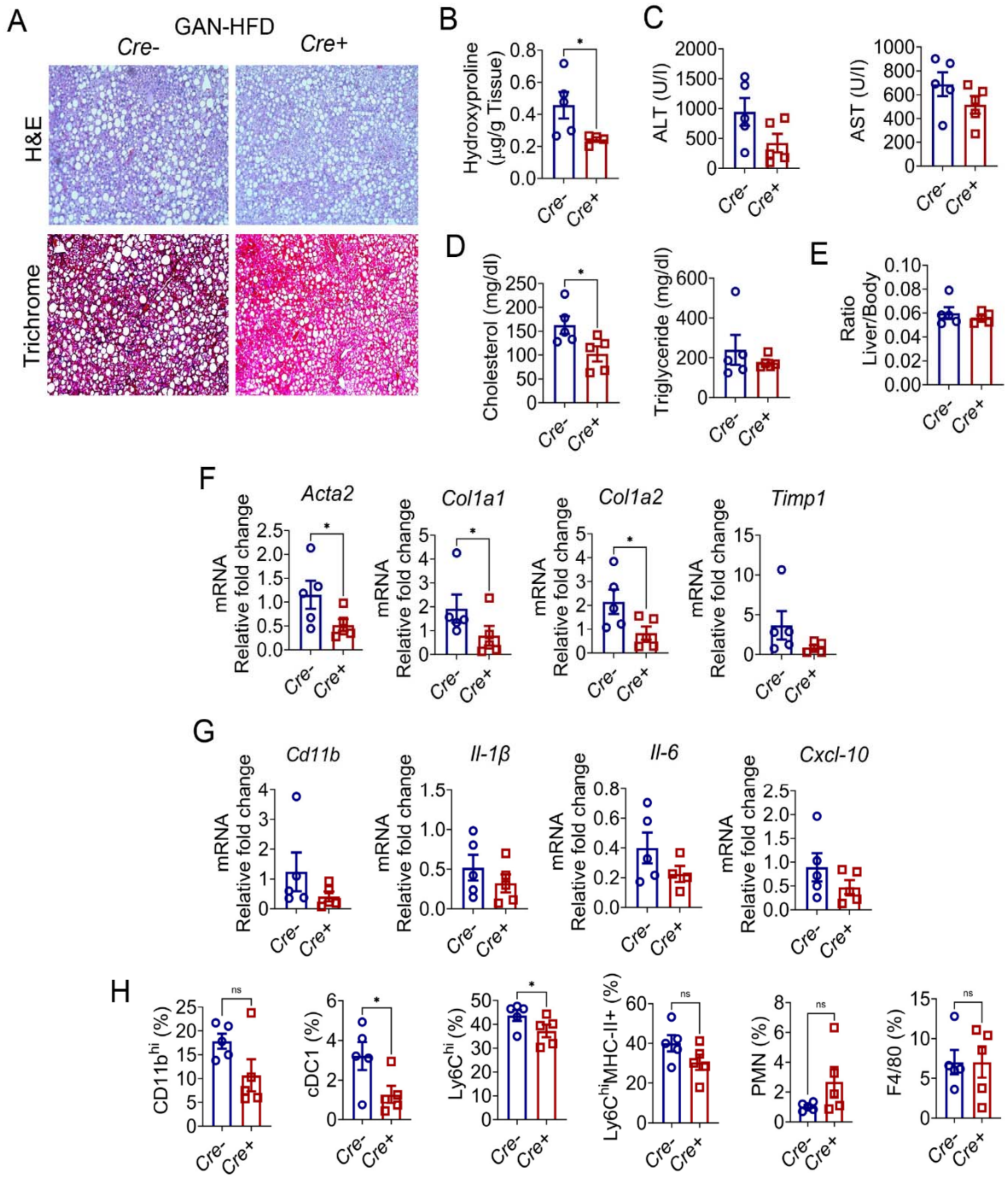

Figure 7: Deletion of *Ephb2* in liver mesenchymal cells when fibrosis is already established attenuates MASH fibrosis. (**A**) Experimental design used to delete

EphB2 in liver mesenchymal cells when fibrosis is already present in *Col1a2Cre*^{ERT2}*/Ephb2*^{WT} (*Col*^{WT}) and *Col1a2Cre*^{ERT2}*/Ephb2*$^{fl/fl}$ (*Col*$^{\Delta Ephb2}$) fed the CDAA-HFD. (**B**) Liver sections of Col^{WT} and Col$^{\Delta Ephb2}$ mice fed the CDAA-HFD for 12 weeks were stained with *H&E* and Masson-Trichrome to assess tissue damage and collagen deposition. (**C**) Plasma levels of liver damage enzymes ALT and AST in *Col*^{WT} and *Col*$^{\Delta Ephb2}$ mice fed the CDAA-HFD (n=4-5 mice/group). (**D**) Plasma level of cholesterol and triglycerides in *Col*^{WT} and *Col*$^{\Delta Ephb2}$ mice fed the CDAA-HFD for 12 weeks (*n* = 4-5 mice/group). (**E**) Level of hydroxyproline quantified in the livers of *Col*^{WT} and *Col*$^{\Delta Ephb2}$ mice fed the CDAA-HFD (n = 4-5 mice/group). (**F**) Liver mRNA level of Ephb2 in *Col*^{WT} and *Col*$^{\Delta Ephb2}$ mice fed the CDAA-HFD (*n* = 5 mice/group, $*p < 0.05$ by Student t test). (**G)** Liver mRNA levels of *Acta2, Col1a1, Col1a2, Col3a1, Col6a2, and Pdgfrβ* in *Col*^{WT} and *Col*$^{\Delta Ephb2}$ mice fed the CDAA-HFD (*n* = 5 mice/group, $*p < 0.05$, $**p < 0.01$ by Student t test). (**H**) Liver mRNA levels of *Cd11b, IL-6 and Tnf-α* in *Col*^{WT} and *Col*$^{\Delta Ephb2}$ mice fed the CDAA-HFD (*n* = 5 mice/group). Data are presented as mean ± SEM, ns = not significant.

Figure 7

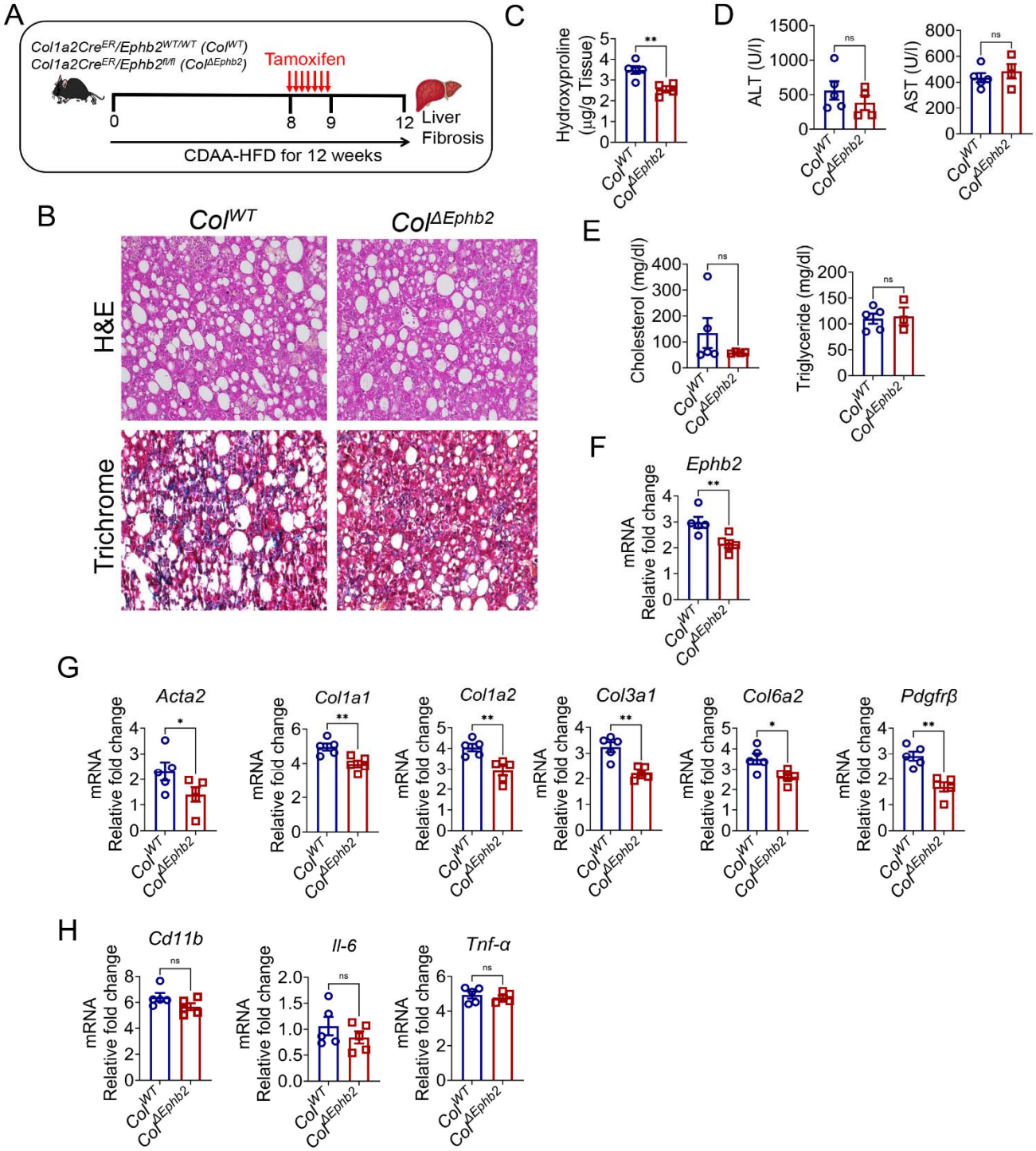

Supplementary figures legends

Figure S1: EphB2 expression is upregulated in human and murine MASH fibrosis. (**A**) Analysis of human MASLD/MASH RNA-seq data (GSE130970) showing that *EPHB2* transcript is elevated in advanced MASH (**p* < 0.05 by ANOVA). (**B**) Representative images of liver sections from human with MASLD/MASH at various stage of fibrosis, stained with H&E and phosphoEphB2. Images were taken using a 20x objective. (**C**) Quantification of phosphoEphB2 in liver specimen of human with MASLD/MASH (n =4-10/group, ***p* < 0.01 by ANOVA). (**D**) Analysis of murine MASH RNA-seq data (GSE119340) showing upregulation of liver *Ephb2* transcript in MASH (n=3/group, **p*<0.05 by Student t test). (**E**) Liver mRNA levels of *Ephb2*, *Vim*, *Cd11b* in mice fed the obesogenic GAN diet at week 7, 12, 18, and 26 (n = 3-5 mice/group, **p* < 0.05, ***p*< 0.01, ****p*<0.001, *****p*<0.0001 by ANOVA). (**F**) Representative images of immunohistochemistry of phosphoEphB2 in liver sections of chow and GAN fed mice at week 26. Images were taken using the 10x objectives. (**G**) Western blots images showing proteins levels of EphB2, αSMA and GAPDH in liver samples of chow and CDAA-HFD fed mice for 12 weeks (n=3 mice/group). Data are presented as mean ± SEM, ns = not significant.

Figure S1

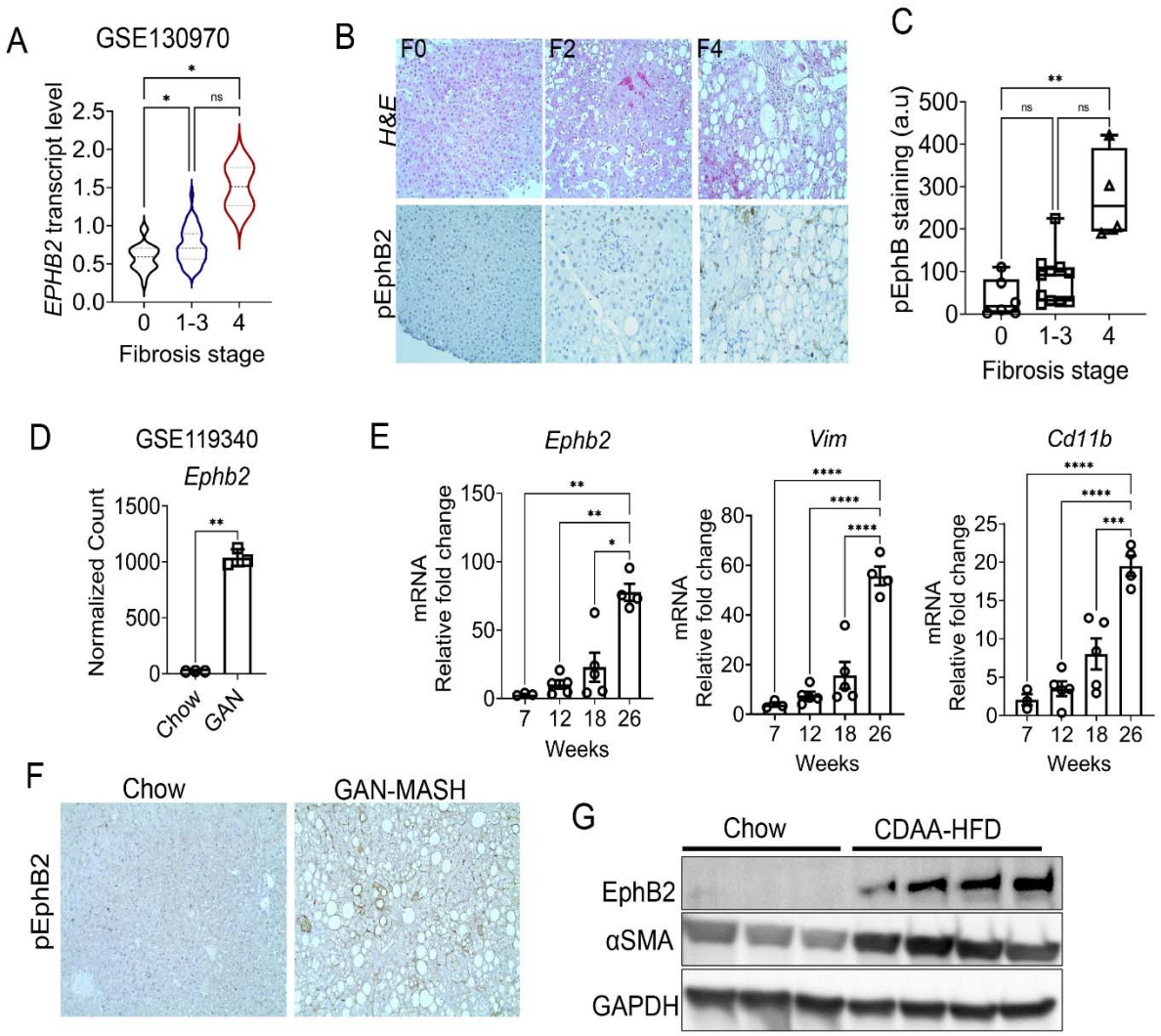

Figure S2: Reduced body weight and improved glucose tolerance in *Ephb2-/-* mice fed the obesogenic GAN diet. (**A**) Body weight gained in *Ephb2+/+* and *Ephb2-/-* mice fed the obesogenic GAN diet for 26 weeks. (**B**) Body weight gained in *Ephb2+/+*

and *Ephb2-/-* mice fed a rodent chow for 26 weeks. (**C**) Liver to body weight ratio in *Ephb2+/+* and *Ephb2-/-* mice fed the GAN diet for 26 weeks. (**D**) Glucose tolerance testing performed in *Ephb2+/+* and *Ephb2-/-* mice fed the obesogenic GAN diet at week 22. Data are presented as mean ± SEM, *$p < 0.05$, **$p < 0.01$, ***$p < 0.001$, ****$p < 0.0001$ by student t test.

Figure S2

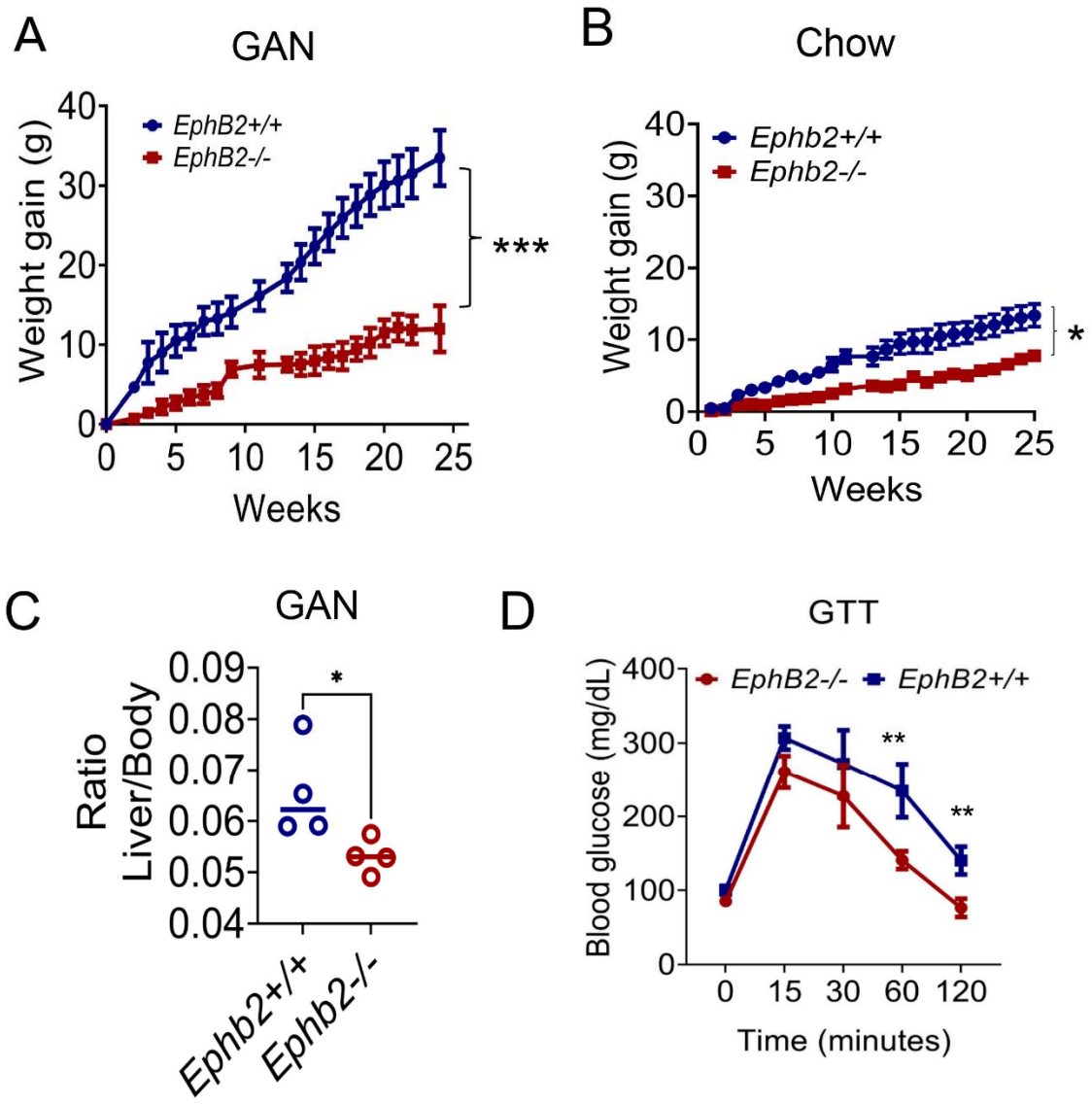

Figure S3: Gating strategy for liver immunophenotyping of myeloid cells in *Ephb2+/+* and *Ephb2-/-* mice fed the GAN and CDAA-HFD. (**A**) Gating strategy used

to identify various immune cells present in the livers of *Ephb2*+/+ and *Ephb2*-/- mice. (**B**) Quantification of hepatic myeloid cells subsets and T (CD3) and B (CD19) cells in the livers of *Ephb2*+/+ and *Ephb2*-/- mice fed the obesogenic GAN diet (n = 5 mice /group, *$p < 0.05$ by student t test). (**C**) Immunophenotyping of macrophages subset (Ly6C, F4/80, PNM-neutrophils) dendritic cells (cDC1) in the livers of *Ephb2*+/+ and *Ephb2*-/- mice fed the non-obesogenic CDAA-HFD for 12 weeks (n=9-10 mice/group, **$p < 0.01$ by Student t test). Data are presented as mean ± SEM, ns = not significant.

Figure S3

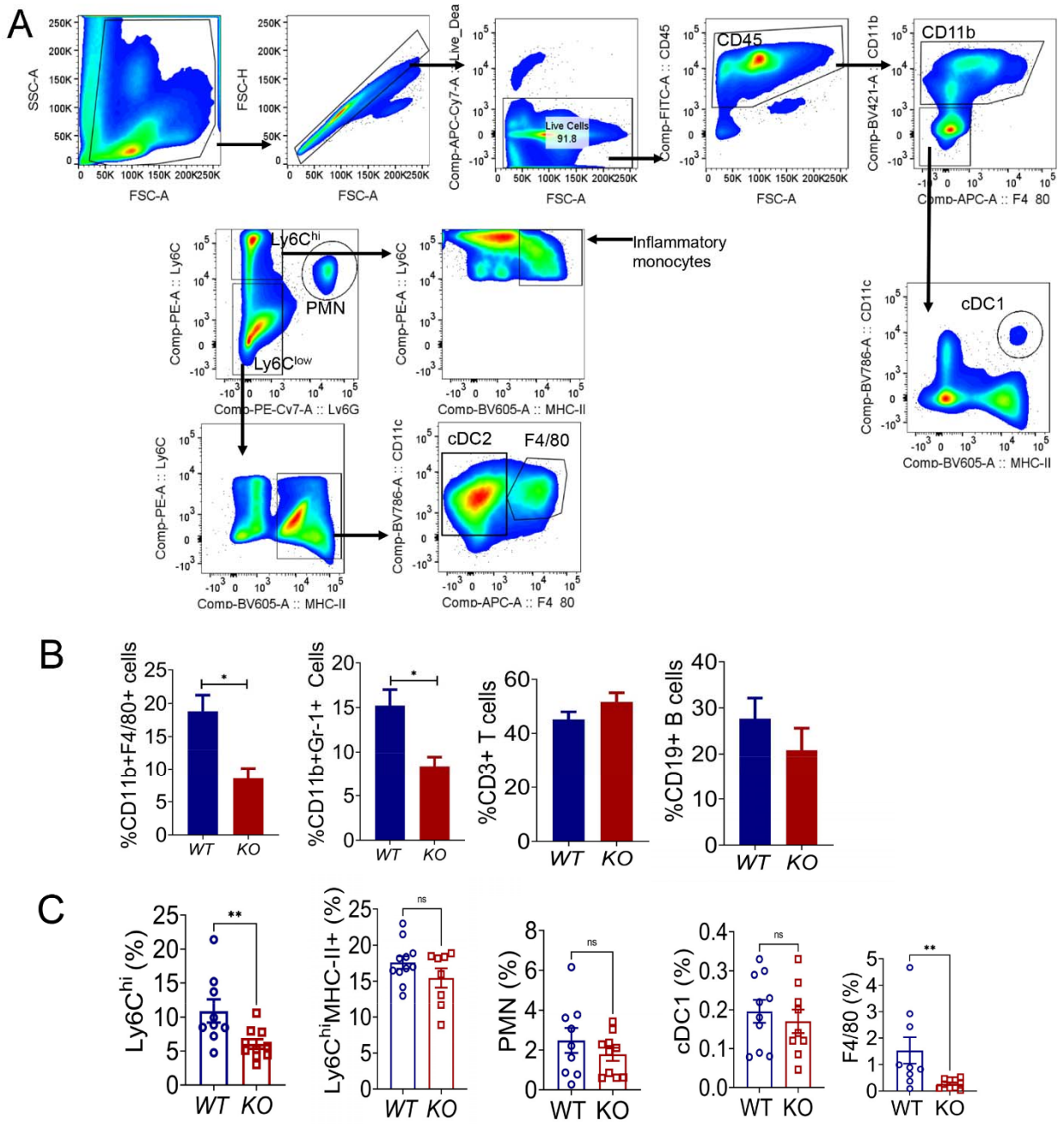

Figure S4: Deletion of *Ephb2* in hepatocyte does not mitigate CDAA-HFD-induced MASH in mice. (**A**) Representative immunofluorescence images of livers sections from

Ephb2$^{fl/fl}$ (Hep^{WT}) and Hep$^{\Delta Ephb2}$ mice fed the CDAA-HFD for 12 weeks, stained with antibodies against EphB2 (red) and Pan-CK (green), with DAPI counterstaining of nuclei in blue. EphB2 fluorescence intensity is reduced in Hep$^{\Delta Ephb2}$ mice fed the CDAA-HFD (**B**) Representative images of liver sections of *Ephb2*$^{fl/fl}$ (Hep^{WT}) and Hep$^{\Delta Ephb2}$ mice fed the CDAA-HFD for 12 weeks, stained with *H&E* and Masson-Trichrome to assess tissue damage and collagen deposition. (**C**) Plasma levels of liver damage enzymes ALT and AST in *Ephb2*$^{fl/fl}$ (Hep^{WT}) and Hep$^{\Delta Ephb2}$ mice fed the CDAA-HFD (n=4-7 mice/group). (**D**) Plasma level of cholesterol and triglycerides in *Ephb2*$^{fl/fl}$ (Hep^{WT}) and Hep$^{\Delta Ephb2}$ mice fed the CDAA-HFD (*n* = 4-7 mice/group). (**E**) Level of hydroxyproline quantified in the livers of *Ephb2*$^{fl/fl}$ (Hep^{WT}) and Hep$^{\Delta Ephb2}$ mice fed the CDAA-HFD (n = 5-7 mice/group). (**F**) Liver to body weight ratio. (**G**) Liver mRNA levels of fibrotic markers *Col1a1, Col1a2, and Acta2* in *Ephb2*$^{fl/fl}$ (Hep^{WT}) and Hep$^{\Delta Ephb2}$ mice fed the CDAA-HFD (*n* = 4-6 mice/group). (**H**) Liver mRNA levels of inflammatory markers *Cd11b, Il-1β, and Il-6* in *Ephb2*$^{fl/fl}$ (Hep^{WT}) and Hep$^{\Delta Ephb2}$ mice fed the CDAA-HFD (*n* = 4-6 mice/group). (**I**) Immunophenotyping of various myeloid cells subsets in the livers of *Ephb2*$^{fl/fl}$ (Hep^{WT}) and Hep$^{\Delta Ephb2}$ mice fed the CDAA-HFD (n=4-7 mice/group). Data are presented as mean ± SEM, ns = not significant.

Figure S4

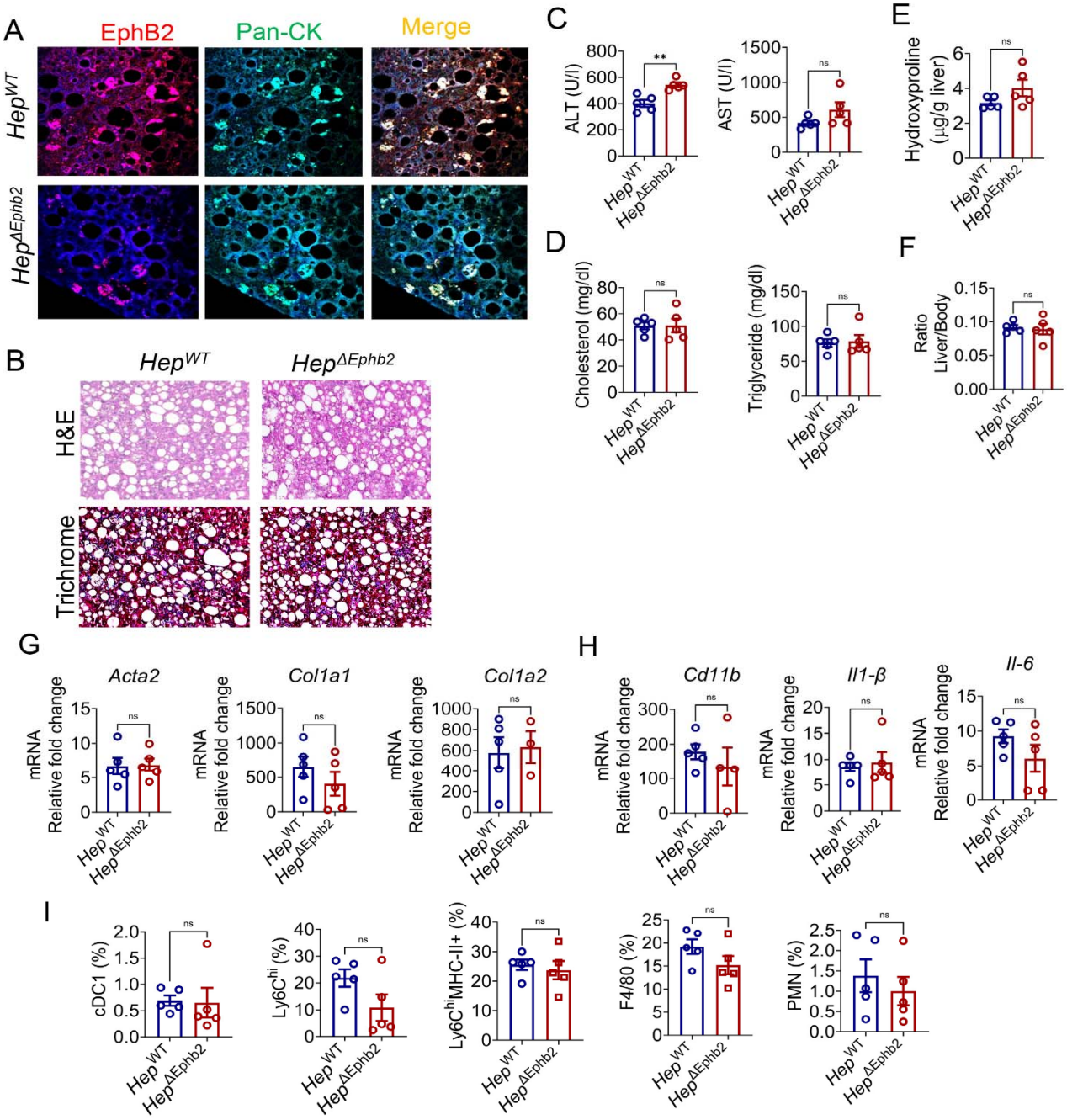

Figure S5: Recombinant human TGF-β2 and TGF-β3 upregulate EPHB2 in primary human hepatic stellate cells. (**A**) Messenger RNA level of *EPHB2*, and *ACTA2* in

TGF-β2 (10ng/ml) stimulated primary human HSCs at various time point (n=3). (***D)*** Western blot showing proteins level of EphB2*, αSMA,* pSmad2/3 Smad2/3 and Vinculin in TGF-β2 stimulated primary human HSCs at various time point. (**C**) Messenger RNA level of *EPHB2*, and *ACTA2* in TGF-β3 stimulated primary human HSCs at various time point (n=3 biological replicate). (**D**) Western blot showing proteins level of EPHB2, αSMA, pSMAD2/3, SMAD2/3 and Vinculin in TGF-β3 (10ng/ml) stimulated primary human HSCs at various time point. Data are presented as mean ± SEM, ns = not significant, *$p < 0.05$, **$p < 0.01$, ***$p<0.001$, ****$p<0.0001$ by ANOVA.

Figure S5

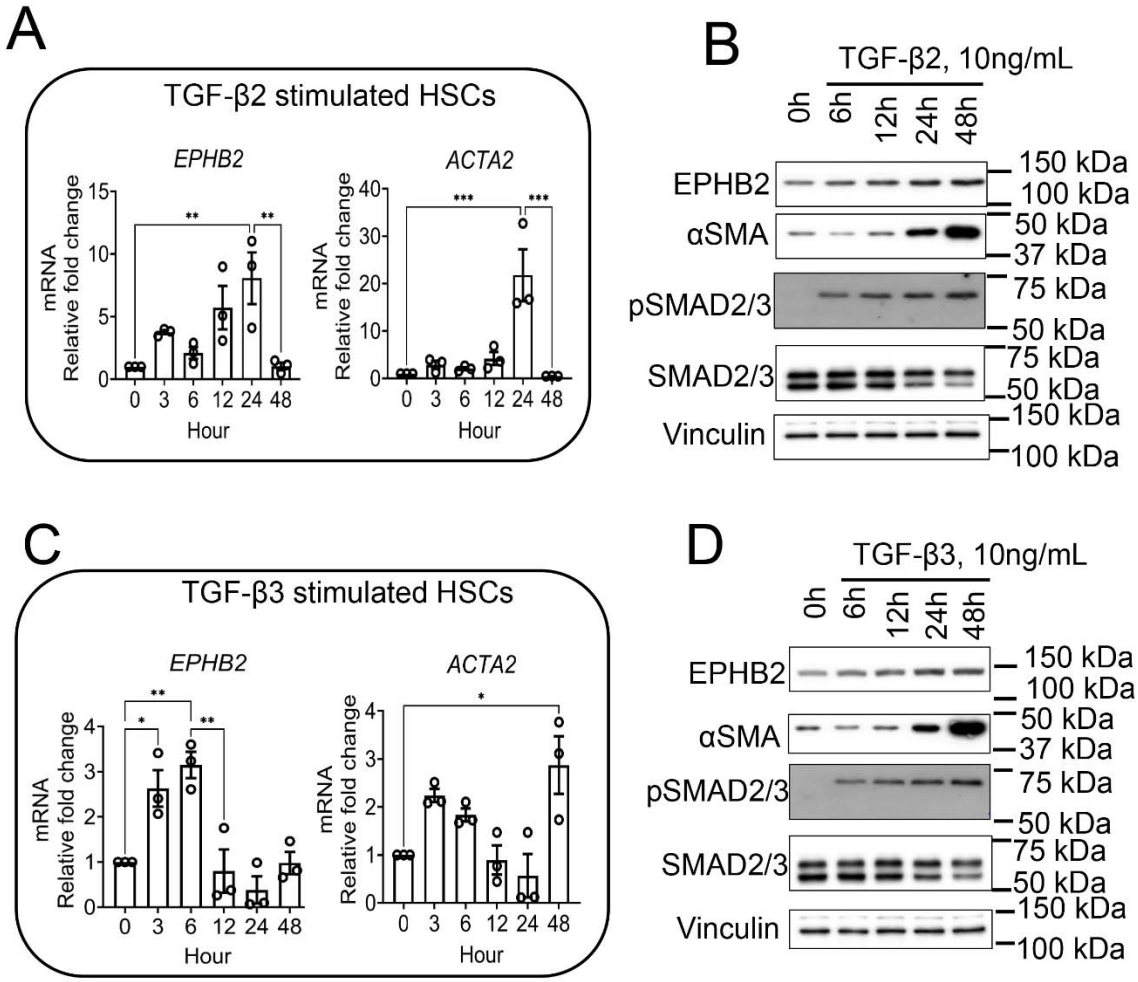

Figure S6: Effects of EPHB2 knocked down in TGFβ1 stimulated human HSCs. (**A**) Messenger RNA levels of *SMAD7*, *SMURF1*, and *SMURF2* measured in different HSCs

lines treated with Mission® *EPHB2*-esiRNA (SIGMA), stimulated with TGF-β1 at 10ng/ml and normalized to the same HSCs lines treated with nontargeting Mission®-esiRNA. (**B**) Quantitative PCR validation of the top fibrogenic genes upregulated in the RNA sequencing data set of TGF-β1-stimulated control HSCs compared to TGF-β1-stimulated *EPHB2*-knocked down HSCs (n=4/group *$p < 0.05$, **$p < 0.01$, ***$p<0.001$, ****$p<0.0001$ by ANOVA).

Figure S6

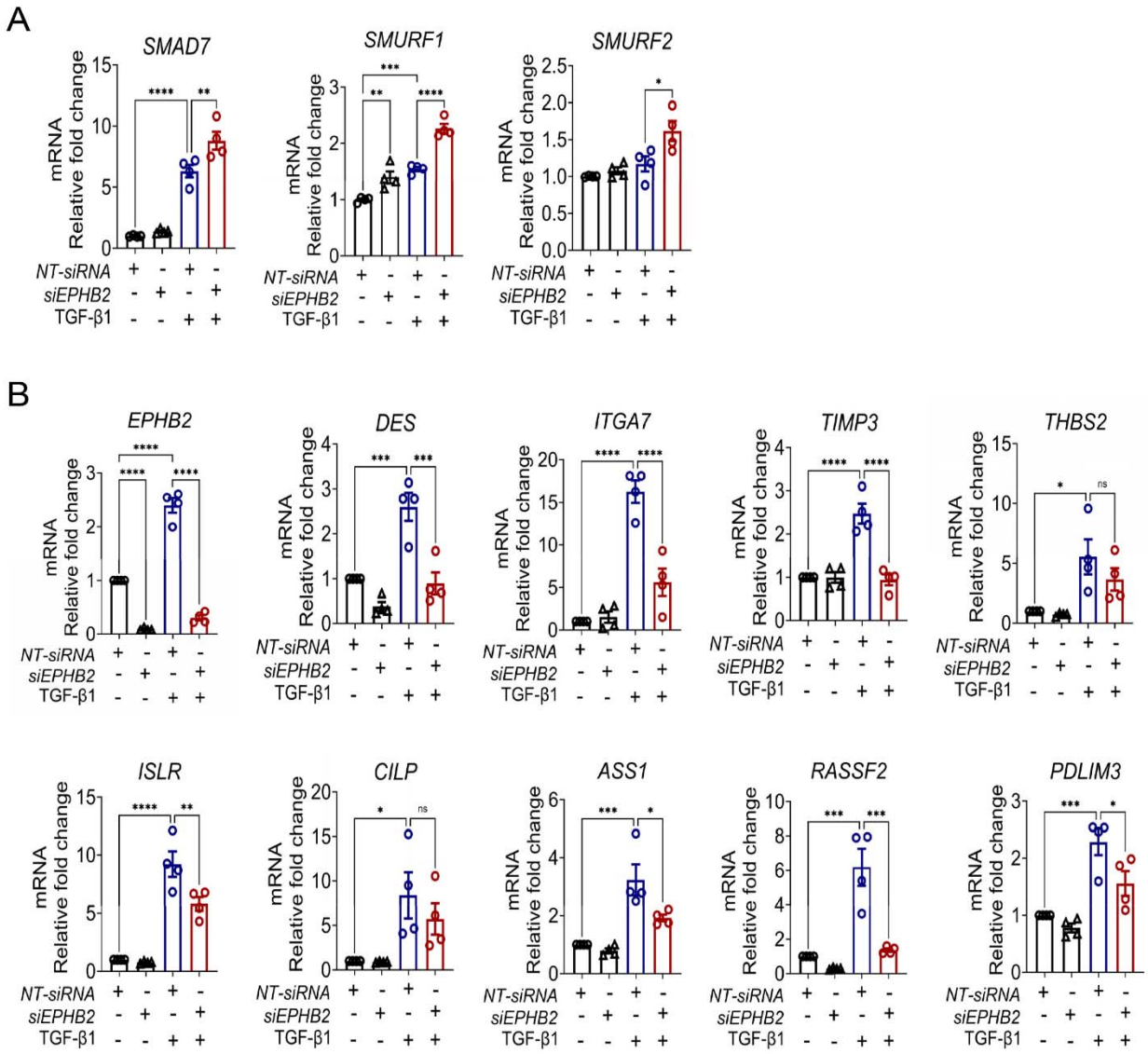

Figure S7: Kinome mapping to identify kinase networks differentially regulated in TGF-β1 stimulated controls and *EPHB2* knocked down human HSCs. Paralogous

relationships between differentially altered kinases in TGF-β1 stimulated controls and *EPHB2* knocked down human HSCs. These HSCs were stimulated with TGF-β1 for 48h. CDKs and MAPKs families of Serine/Threonine kinases were significantly affected by knocking down EPHB2 in TGF-β1 stimulated HSCs.

Figure S7

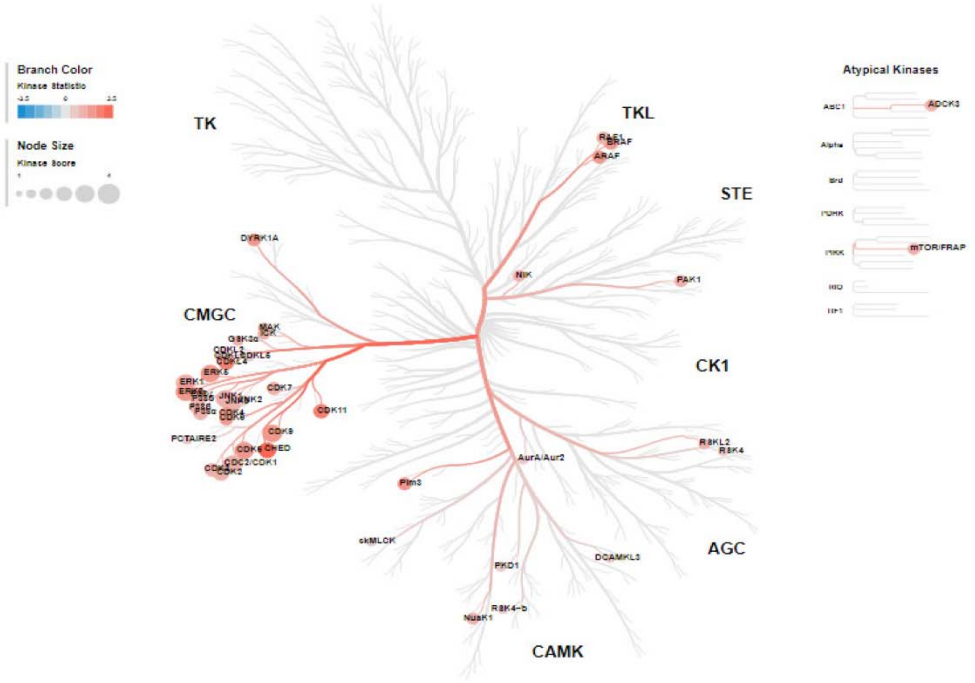

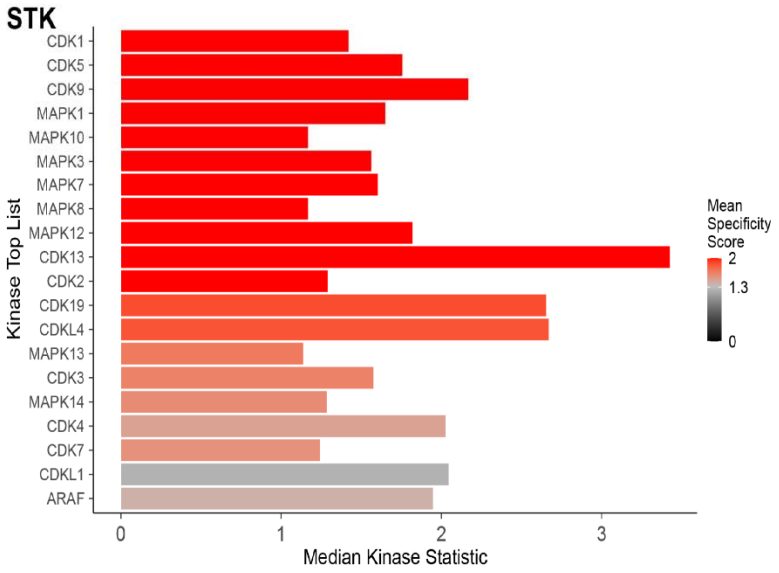

Figure S8: Deletion of Ephb2 in HSCs attenuates CCl_4-induced hepatic fibrosis. *EphB2*$^{fl/fl}$ mice (Cre-) were crossed with the tamoxifen-inducible *Col1a2Cre*^{ERT2} mice to

generate *Col1a2Cre*^{ERT2}*/Ephb2*$^{fl/fl}$ (Cre+) lines. (**A**) Representative images of liver sections of Cre- and Cre+ mice treated with CCl_4 for 4 weeks, stained with *H&E* and Masson-Trichrome to assess tissue damage and collagen deposition. (**B**) Level of hydroxyproline quantified in the livers of Cre- and Cre+ mice treated with CCl_4 for 4 weeks (n = 6-9 mice/group, *$p < 0.05$ by Student's t test). (**C**) Plasma levels of liver damage enzymes ALT and AST in Cre- and Cre+ mice treated with CCl_4 for 4 weeks (n =6-10 mice/group). (**D**) Liver mRNA levels of *Col1a1, Fn, Acta2, and Timp1* in Cre- and Cre+ mice receiving CCl4 for 4 weeks (*n* = 6-9 mice/group, *$p < 0.05$, **$p < 0.01$ by Student t test). (**E**) Liver mRNA levels of *Cd11b, Ccl-5, Cxcl-10, and Il-1β* in Cre- and Cre+ mice receiving CCl_4 for 4 weeks (*n* = 6-9 mice/group, *$p < 0.05$, **$p < 0.01$ by Student t test). (**F**) Immunophenotyping of T cell (CD3), B cells (CD19), and macrophages subset (Ly6C, F4/80, PMN,) in the livers of Cre- and Cre+ mice receiving CCl_4 for 4 weeks (n = 6-9 mice/group, *$p < 0.05$ by Student's t test). Data are presented as mean ± SEM, ns = not significant.

Figure S8

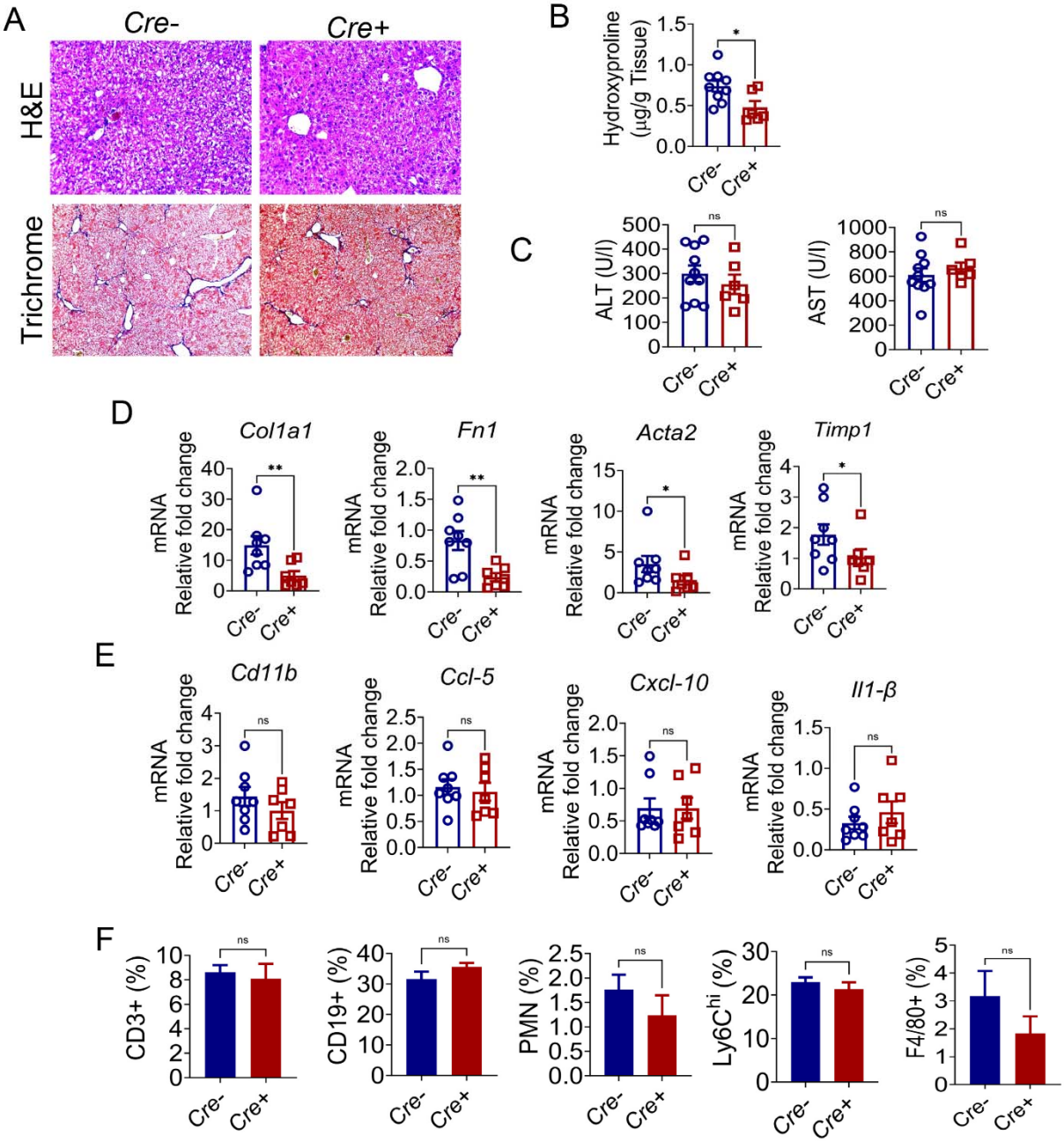
A
Cre-
Cre+
H&E
Trichrome
B
Hydroxyproline (μg/g Tissue)
C
ALT (U/l)
AST (U/l)
ns
D
Col1a1
Fn1
Acta2
Timp1
mRNA Relative fold change
E
Cd11b
Ccl-5
Cxcl-10
Il1-β
F
CD3+ (%)
CD19+ (%)
PMN (%)
Ly6C^hi (%)
F4/80+ (%)

References

Alack, K., Weiss, A., Krüger, K., Höret, M., Schermuly, R., Frech, T., Eggert, M., & Mooren, F. C. (2020). Profiling of human lymphocytes reveals a specific network of protein kinases modulated by endurance training status. *Sci Rep*, *10*(1), 888. https://doi.org/10.1038/s41598-020-57676-6

Chirumamilla, C. S., Fazil, M., Perez-Novo, C., Rangarajan, S., de Wijn, R., Ramireddy, P., Verma, N. K., & Vanden Berghe, W. (2019). Profiling Activity of Cellular Kinases in Migrating T-Cells. *Methods Mol Biol*, *1930*, 99-113. https://doi.org/10.1007/978-1-4939-9036-8_13

Coulthard, M. G., Morgan, M., Woodruff, T. M., Arumugam, T. V., Taylor, S. M., Carpenter, T. C., Lackmann, M., & Boyd, A. W. (2012). Eph/Ephrin Signaling in Injury and Inflammation. *The American Journal of Pathology*, *181*(5), 1493-1503. https://doi.org/http://dx.doi.org/10.1016/j.ajpath.2012.06.043

Ding, N., Yu, Ruth T., Subramaniam, N., Sherman, Mara H., Wilson, C., Rao, R., Leblanc, M., Coulter, S., He, M., Scott, C., Lau, Sue L., Atkins, Annette R., Barish, Grant D., Gunton, Jenny E., Liddle, C., Downes, M., & Evans, Ronald M. (2013). A Vitamin D Receptor/SMAD Genomic Circuit Gates Hepatic Fibrotic Response. *Cell*, *153*(3), 601-613. https://doi.org/http://dx.doi.org/10.1016/j.cell.2013.03.028

Dobin, A., Davis, C. A., Schlesinger, F., Drenkow, J., Zaleski, C., Jha, S., Batut, P., Chaisson, M., & Gingeras, T. R. (2013). STAR: ultrafast universal RNA-seq aligner. *Bioinformatics*, *29*(1), 15-21. https://doi.org/10.1093/bioinformatics/bts635

Egal, E. S. A., Kamdem, S. D., Yoshigi, M., Yang, C. C., Pellizzari, S., Kameni, E. M., Helms, M. N., Assassi, S., Henkemeyer, M., Frech, T. M., & Mimche, P. N. (2024). EphB2 Receptor Promotes Dermal Fibrosis in Systemic Sclerosis. *Arthritis Rheumatol*, *76*(8), 1303-1316. https://doi.org/10.1002/art.42858

Ewels, P., Magnusson, M., Lundin, S., & Käller, M. (2016). MultiQC: summarize analysis results for multiple tools and samples in a single report. *Bioinformatics*, *32*(19), 3047-3048. https://doi.org/10.1093/bioinformatics/btw354

Frangogiannis, N. G. (2020). Transforming growth factor–β in tissue fibrosis. *Journal of Experimental Medicine*, *217*(3). https://doi.org/10.1084/jem.20190103

Friedman, S. L. (2008). Mechanisms of Hepatic Fibrogenesis. *Gastroenterology*, *134*(6), 1655-1669. https://doi.org/http://dx.doi.org/10.1053/j.gastro.2008.03.003

Gao, Q., Liu, W., Cai, J., Li, M., Gao, Y., Lin, W., & Li, Z. (2014). EphB2 promotes cervical cancer progression by inducing epithelial-mesenchymal transition. *Human Pathology*, *45*(2), 372-381. https://doi.org/http://dx.doi.org/10.1016/j.humpath.2013.10.001

Genander, M., Halford, M. M., Xu, N. J., Eriksson, M., Yu, Z., Qiu, Z., Martling, A., Greicius, G., Thakar, S., Catchpole, T., Chumley, M. J., Zdunek, S., Wang, C., Holm, T., Goff, S. P., Pettersson, S., Pestell, R. G., Henkemeyer, M., & Frisén, J. (2009). Dissociation of EphB2 signaling pathways mediating progenitor cell proliferation and tumor suppression. *Cell*, *139*(4), 679-692. https://doi.org/10.1016/j.cell.2009.08.048

Giannopoulos, K., Karikis, I., Byrd, C., Sanidas, G., Wolff, N., Triantafyllou, M., Simonti, G., Vidva, R., Koutroulis, I., Theocharis, S., & Kratimenos, P. (2025). Eph/ephrin-

mediated immune modulation: a potential therapeutic target. *Front Immunol*, *16*, 1539567. https://doi.org/10.3389/fimmu.2025.1539567

Hagström, H., Nasr, P., Ekstedt, M., Hammar, U., Stål, P., Hultcrantz, R., & Kechagias, S. (2017). Fibrosis stage but not NASH predicts mortality and time to development of severe liver disease in biopsy-proven NAFLD. *Journal of Hepatology*, *67*(6), 1265-1273. https://doi.org/https://doi.org/10.1016/j.jhep.2017.07.027

Harrison, S. A., Bedossa, P., Guy, C. D., Schattenberg, J. M., Loomba, R., Taub, R., Labriola, D., Moussa, S. E., Neff, G. W., Rinella, M. E., Anstee, Q. M., Abdelmalek, M. F., Younossi, Z., Baum, S. J., Francque, S., Charlton, M. R., Newsome, P. N., Lanthier, N., Schiefke, I.,…Ratziu, V. (2024). A Phase 3, Randomized, Controlled Trial of Resmetirom in NASH with Liver Fibrosis. *N Engl J Med*, *390*(6), 497-509. https://doi.org/10.1056/NEJMoa2309000

Hata, A., & Chen, Y. G. (2016). TGF-β Signaling from Receptors to Smads. *Cold Spring Harb Perspect Biol*, *8*(9). https://doi.org/10.1101/cshperspect.a022061

Henderson, N. C., Arnold, T. D., Katamura, Y., Giacomini, M. M., Rodriguez, J. D., McCarty, J. H., Pellicoro, A., Raschperger, E., Betsholtz, C., Ruminski, P. G., Griggs, D. W., Prinsen, M. J., Maher, J. J., Iredale, J. P., Lacy-Hulbert, A., Adams, R. H., & Sheppard, D. (2013). Targeting of [alpha]v integrin identifies a core molecular pathway that regulates fibrosis in several organs [Article]. *Nat Med*, *19*(12), 1617-1624. https://doi.org/10.1038/nm.3282

http://www.nature.com/nm/journal/v19/n12/abs/nm.3282.html#supplementary-information

Henkemeyer, M., Orioli, D., Henderson, J. T., Saxton, T. M., Roder, J., Pawson, T., & Klein, R. (1996). Nuk Controls Pathfinding of Commissural Axons in the Mammalian Central Nervous System. *Cell*, *86*(1), 35-46. https://doi.org/http://dx.doi.org/10.1016/S0092-8674(00)80075-6

Hilhorst, R., Houkes, L., van den Berg, A., & Ruijtenbeek, R. (2009). Peptide microarrays for detailed, high-throughput substrate identification, kinetic characterization, and inhibition studies on protein kinase A. *Anal Biochem*, *387*(2), 150-161. https://doi.org/10.1016/j.ab.2009.01.022

Hoang, S. A., Oseini, A., Feaver, R. E., Cole, B. K., Asgharpour, A., Vincent, R., Siddiqui, M., Lawson, M. J., Day, N. C., Taylor, J. M., Wamhoff, B. R., Mirshahi, F., Contos, M. J., Idowu, M., & Sanyal, A. J. (2019). Gene Expression Predicts Histological Severity and Reveals Distinct Molecular Profiles of Nonalcoholic Fatty Liver Disease. *Scientific Reports*, *9*(1), 12541. https://doi.org/10.1038/s41598-019-48746-5

Holmberg, J., Genander, M., Halford, M. M., Annerén, C., Sondell, M., Chumley, M. J., Silvany, R. E., Henkemeyer, M., & Frisén, J. (2006). EphB receptors coordinate migration and proliferation in the intestinal stem cell niche. *Cell*, *125*(6), 1151-1163. https://doi.org/10.1016/j.cell.2006.04.030

Huang, Z., Liu, S., Tang, A., Al-Rabadi, L., Henkemeyer, M., Mimche, P. N., & Huang, Y. (2021). Key role for EphB2 receptor in kidney fibrosis. *Clin Sci (Lond)*, *135*(17), 2127-2142. https://doi.org/10.1042/cs20210644

Kania, A., & Klein, R. (2016). Mechanisms of ephrin-Eph signalling in development, physiology and disease [Review]. *Nat Rev Mol Cell Biol*, *17*(4), 240-256. https://doi.org/10.1038/nrm.2015.16

Kechin, A., Boyarskikh, U., Kel, A., & Filipenko, M. (2017). cutPrimers: A New Tool for Accurate Cutting of Primers from Reads of Targeted Next Generation Sequencing. *J Comput Biol*, *24*(11), 1138-1143. https://doi.org/10.1089/cmb.2017.0096

Kisseleva, T. (2017). The origin of fibrogenic myofibroblasts in fibrotic liver. *Hepatology*, n/a-n/a. https://doi.org/10.1002/hep.28948

Kleiner, D. E., & Brunt, E. M. (2012). Nonalcoholic fatty liver disease: pathologic patterns and biopsy evaluation in clinical research. *Semin Liver Dis*, *32*(1), 3-13. https://doi.org/10.1055/s-0032-1306421

Koyama, Y., & Brenner, D. A. (2017). Liver inflammation and fibrosis. *J Clin Invest*, *127*(1), 55-64. https://doi.org/10.1172/jci88881

Krämer, A., Green, J., Pollard, J., Jr., & Tugendreich, S. (2014). Causal analysis approaches in Ingenuity Pathway Analysis. *Bioinformatics*, *30*(4), 523-530. https://doi.org/10.1093/bioinformatics/btt703

Liao, Y., Smyth, G. K., & Shi, W. (2014). featureCounts: an efficient general purpose program for assigning sequence reads to genomic features. *Bioinformatics*, *30*(7), 923-930. https://doi.org/10.1093/bioinformatics/btt656

Love, M. I., Huber, W., & Anders, S. (2014). Moderated estimation of fold change and dispersion for RNA-seq data with DESeq2. *Genome Biol*, *15*(12), 550. https://doi.org/10.1186/s13059-014-0550-8

Mimche, P. N., Brady, L. M., Bray, C. F., Lee, C. M., Thapa, M., King, T. P., Quicke, K., McDermott, C. D., Mimche, S. M., Grakoui, A., Morgan, E. T., & Lamb, T. J. (2015). The receptor tyrosine kinase EphB2 promotes hepatic fibrosis in mice. *Hepatology*, *62*(3), 900-914. https://doi.org/10.1002/hep.27792

Mimche, P. N., Lee, C. M., Mimche, S. M., Thapa, M., Grakoui, A., Henkemeyer, M., & Lamb, T. J. (2018). EphB2 receptor tyrosine kinase promotes hepatic fibrogenesis in mice via activation of hepatic stellate cells. *Scientific Reports*, *8*(1), 2532. https://doi.org/10.1038/s41598-018-20926-9

Miyazawa, K., & Miyazono, K. (2017). Regulation of TGF-β Family Signaling by Inhibitory Smads. *Cold Spring Harb Perspect Biol*, *9*(3). https://doi.org/10.1101/cshperspect.a022095

Muzurović, E., Haluzik, M., Horváth, L., Vlacho, B., & Mauricio, D. (2025). Incretin-based Agents and Metabolic Dysfunction-associated Steatotic Liver Disease. *Curr Pharm Des*. https://doi.org/10.2174/0113816128378484250619080753

Newsome, P. N., & Loomba, R. (2025). Therapeutic horizons in metabolic dysfunction-associated steatohepatitis. *J Clin Invest*, *135*(13). https://doi.org/10.1172/jci186425

Pasquale, E. B. (2008). Eph-Ephrin Bidirectional Signaling in Physiology and Disease. *Cell*, *133*(1), 38-52. https://doi.org/http://dx.doi.org/10.1016/j.cell.2008.03.011

Radhakrishnan, S., Ke, J. Y., & Pellizzon, M. A. (2020). Targeted Nutrient Modifications in Purified Diets Differentially Affect Nonalcoholic Fatty Liver Disease and Metabolic Disease Development in Rodent Models. *Curr Dev Nutr*, *4*(6), nzaa078. https://doi.org/10.1093/cdn/nzaa078

Radhakrishnan, S., Yeung, S. F., Ke, J. Y., Antunes, M. M., & Pellizzon, M. A. (2021). Considerations When Choosing High-Fat, High-Fructose, and High-Cholesterol Diets to Induce Experimental Nonalcoholic Fatty Liver Disease in Laboratory Animal Models. *Curr Dev Nutr*, *5*(12), nzab138. https://doi.org/10.1093/cdn/nzab138

Reddy, G. K., & Enwemeka, C. S. (1996). A simplified method for the analysis of hydroxyproline in biological tissues. *Clin Biochem*, *29*(3), 225-229. https://doi.org/10.1016/0009-9120(96)00003-6

Sanyal, A. J., Newsome, P. N., Kliers, I., Østergaard, L. H., Long, M. T., Kjær, M. S., Cali, A. M. G., Bugianesi, E., Rinella, M. E., Roden, M., & Ratziu, V. (2025). Phase 3 Trial of Semaglutide in Metabolic Dysfunction-Associated Steatohepatitis. *N Engl J Med*, *392*(21), 2089-2099. https://doi.org/10.1056/NEJMoa2413258

Son, G., Hines, I. N., Lindquist, J., Schrum, L. W., & Rippe, R. A. (2009). Inhibition of phosphatidylinositol 3-kinase signaling in hepatic stellate cells blocks the progression of hepatic fibrosis. *Hepatology*, *50*(5), 1512-1523. https://doi.org/10.1002/hep.23186

Sun, T., Huang, Z., Liang, W. C., Yin, J., Lin, W. Y., Wu, J., Vernes, J. M., Lutman, J., Caplazi, P., Jeet, S., Wong, T., Wong, M., DePianto, D. J., Morshead, K. B., Sun, K. H., Modrusan, Z., Vander Heiden, J. A., Abbas, A. R., Zhang, H.,…Arron, J. R. (2021). TGFβ2 and TGFβ3 isoforms drive fibrotic disease pathogenesis. *Sci Transl Med*, *13*(605). https://doi.org/10.1126/scitranslmed.abe0407

Targher, G., Lonardo, A., & Byrne, C. D. (2017). Nonalcoholic fatty liver disease and chronic vascular complications of diabetes mellitus [Review Article]. *Nature Reviews Endocrinology*, *14*, 99. https://doi.org/10.1038/nrendo.2017.173

https://www.nature.com/articles/nrendo.2017.173#supplementary-information

Wang, S., Li, K., Pickholz, E., Dobie, R., Matchett, K. P., Henderson, N. C., Carrico, C., Driver, I., Borch Jensen, M., Chen, L., Petitjean, M., Bhattacharya, D., Fiel, M. I., Liu, X., Kisseleva, T., Alon, U., Adler, M., Medzhitov, R., & Friedman, S. L. (2023). An autocrine signaling circuit in hepatic stellate cells underlies advanced fibrosis in nonalcoholic steatohepatitis. *Sci Transl Med*, *15*(677), eadd3949. https://doi.org/10.1126/scitranslmed.add3949

Wang, X., Spandidos, A., Wang, H., & Seed, B. (2012). PrimerBank: a PCR primer database for quantitative gene expression analysis, 2012 update. *Nucleic Acids Res*, *40*(Database issue), D1144-1149. https://doi.org/10.1093/nar/gkr1013

Wells, R. G., & Schwabe, R. F. (2015). Origin and Function of Myofibroblasts in the Liver. *Semin Liver Dis*, *35*(02), e1-e1. https://doi.org/10.1055/s-0035-1554915

Wu, B., Rockel, J. S., Lagares, D., & Kapoor, M. (2019). Ephrins and Eph Receptor Signaling in Tissue Repair and Fibrosis [journal article]. *Current Rheumatology Reports*, *21*(6), 23. https://doi.org/10.1007/s11926-019-0825-x

Xiao, Y., Batmanov, K., Hu, W., Zhu, K., Tom, A. Y., Guan, D., Jiang, C., Cheng, L., McCright, S. J., Yang, E. C., Lanza, M. R., Liu, Y., Hill, D. A., & Lazar, M. A. (2023). Hepatocytes demarcated by EphB2 contribute to the progression of nonalcoholic steatohepatitis. *Sci Transl Med*, *15*(682), eadc9653. https://doi.org/10.1126/scitranslmed.adc9653

Xiong, X., Kuang, H., Ansari, S., Liu, T., Gong, J., Wang, S., Zhao, X.-Y., Ji, Y., Li, C., Guo, L., Zhou, L., Chen, Z., Leon-Mimila, P., Chung, M. T., Kurabayashi, K., Opp, J., Campos-Pérez, F., Villamil-Ramírez, H., Canizales-Quinteros, S.,…Lin, J. D. (2019). Landscape of Intercellular Crosstalk in Healthy and NASH Liver Revealed by Single-Cell Secretome Gene Analysis. *Molecular Cell*, *75*(3), 644-660.e645. https://doi.org/https://doi.org/10.1016/j.molcel.2019.07.028

Younossi, Z., Anstee, Q. M., Marietti, M., Hardy, T., Henry, L., Eslam, M., George, J., & Bugianesi, E. (2017). Global burden of NAFLD and NASH: trends, predictions, risk factors and prevention [Review Article]. *Nature Reviews Gastroenterology &Amp; Hepatology*, *15*, 11. https://doi.org/10.1038/nrgastro.2017.109

https://www.nature.com/articles/nrgastro.2017.109#supplementary-information

Younossi, Z. M., Stepanova, M., Rafiq, N., Henry, L., Loomba, R., Makhlouf, H., & Goodman, Z. (2017). Nonalcoholic steatofibrosis independently predicts mortality in nonalcoholic fatty liver disease. *Hepatol Commun*, *1*(5), 421-428. https://doi.org/10.1002/hep4.1054

Younossi, Z. M., Zelber-Sagi, S., Lazarus, J. V., Wong, V. W., Yilmaz, Y., Duseja, A., Eguchi, Y., Castera, L., Pessoa, M. G., Oliveira, C. P., El-Kassas, M., Tsochatzis, E., Fan, J. G., Spearman, C. W., Tacke, F., Castellanos Fernandez, M. I., Alkhouri, N., Schattenberg, J. M., Romero-Gómez, M.,…Alqahtani, S. A. (2025). Global Consensus Recommendations for Metabolic Dysfunction-Associated Steatotic Liver Disease and Steatohepatitis. *Gastroenterology*. https://doi.org/10.1053/j.gastro.2025.02.044